Enucleated cells reveal differential roles of the nucleus in cell migration, polarity, and mechanotransduction

David M. Graham,[1,2] Tomas Andersen,[5] Lisa Sharek,[1] Gunes Uzer,[4,6] Katheryn Rothenberg,[7] Brenton D. Hoffman,[7] Janet Rubin,[4] Martial Balland,[5] James E. Bear,[1,2] and Keith Burridge[1,2,3]

[1]Department of Cell Biology and Physiology, [2]UNC Lineberger Comprehensive Cancer Center, [3]McAllister Heart Institute, and [4]Department of Medicine, University of North Carolina at Chapel Hill, Chapel Hill, NC
[5]Laboratoire Interdisciplinaire de Physique, Université Grenoble Alpes, Grenoble, France
[6]Department of Mechanical and Biomedical Engineering, Boise State University, Boise, ID
[7]Department of Biomedical Engineering, Duke University, Durham, NC

The nucleus has long been postulated to play a critical physical role during cell polarization and migration, but that role has not been defined or rigorously tested. Here, we enucleated cells to test the physical necessity of the nucleus during cell polarization and directed migration. Using enucleated mammalian cells (cytoplasts), we found that polarity establishment and cell migration in one dimension (1D) and two dimensions (2D) occur without the nucleus. Cytoplasts directionally migrate toward soluble (chemotaxis) and surface-bound (haptotaxis) extracellular cues and migrate collectively in scratch-wound assays. Consistent with previous studies, migration in 3D environments was dependent on the nucleus. In part, this likely reflects the decreased force exerted by cytoplasts on mechanically compliant substrates. This response is mimicked both in cells with nucleocytoskeletal defects and upon inhibition of actomyosin-based contractility. Together, our observations reveal that the nucleus is dispensable for polarization and migration in 1D and 2D but critical for proper cell mechanical responses.

Introduction

The nuclear functions of DNA replication and gene regulation are well known, but the nucleus also plays less understood physical roles where its presence within the cell and connection to the cytoskeleton are thought to be important in cell polarization and cell migration. In both processes, active positioning of the nucleus imparts dynamic structural and functional organization within the cell that ultimately influences cell behavior. Aberrant positioning of the nucleus can lead to developmental defects (Zhang et al., 2009) and impair cellular function (Metzger et al., 2012) and is seen in several human diseases (Gundersen and Worman, 2013). A more recent and equally important physical role of the nucleus has been ascribed to mechanical signaling within the cell. Here, the degree of structural integration of the nucleus within the cell is postulated to be crucial for regulating how cells sense and respond to force (Jaalouk and Lammerding, 2009).

During polarity establishment and cell migration, the nucleus is actively positioned in many cell types. For example, in fibroblasts, rearward nuclear movement allows anterior orientation of the centrosome, promoting anterior–posterior polarity of the cell in 2D (Gomes et al., 2005). In cells migrating in 3D that exhibit unidirectional polarity, the nucleus can be actively repositioned to act as an intracellular piston to facilitate migration (Petrie et al., 2014). Molecular motors, cytoskeletal

elements, and cell adhesions are structurally connected within the cytoskeletal system as a whole, and it is thought that each contributes to tensional homeostasis of the cell (DuFort et al., 2011). In light of this, aberrant force transmission between the cytoskeleton and nucleus has been suggested as the underlying cause for defective nuclear positioning (Graham and Burridge, 2016). It is, however, unclear how the position of the nucleus conversely regulates mechanical signaling within the cell to collectively affect these processes. How would removal of the nucleus affect force transmission within the cell?

Recent work has dramatically expanded our understanding of the molecular underpinnings of the mechanical linkages that connect the nucleus to cytoskeletal elements of the cytoplasm. Forces are transmitted through the linker of nucleoskeleton and cytoskeleton (LINC) complex (Crisp et al., 2006), where the inner nuclear membrane proteins Sun1 and Sun2 directly bind with outer nuclear membrane Nesprin proteins in the lumen of the nuclear envelope. Nesprin proteins span the outer nuclear membrane to associate with the cytoskeleton and associated motors, whereas Sun proteins associate with lamin A/C, nuclear pore complexes, and other proteins within the nucleus (Borrego-Pinto et al., 2012). This chain of protein interactions

Correspondence to James E. Bear: jbear@email.unc.edu; Keith Burridge: keith_burridge@med.unc.edu

allows forces to be exerted on the nucleus and is responsible for rapid strain-stiffening of the nucleus in response to extrinsic force (Guilluy et al., 2014). In addition to applied forces, intrinsic cell-derived forces can transmit through dorsal actin stress fibers to the LINC complex, allowing posterior positioning of the nucleus via actin retrograde flow (Luxton et al., 2010). Because cell-derived forces are highly dependent on the mechanical properties of the microenvironment, the LINC complex likely plays an important role in regulating the response of the cell to environmental rigidity. This was shown for rigidity-dependent nuclear localization of YAP (Elosegui-Artola et al., 2017). Together, these and many other recent studies demonstrate the intricate network of molecular connections that help position the nucleus and make it sensitive to mechanical cues.

Several studies have reported defects in cell polarity, migration, and mechanotransduction upon disruption of nucleoskeletal connections. It is unclear what role the nucleus plays during these processes and how they are affected by nuclear loss as opposed to aberrant nuclear positioning. Cellular enucleation is an older approach that has been used to explore migration in the absence of the nucleus (Goldman et al., 1973; Shaw and Bray, 1977; Euteneuer and Schliwa, 1984, 1992; Verkhovsky et al., 1999). We revisited this technique to study the role of the nucleus in cell polarity and distinct forms of migration (e.g., in 1D, 2D, and 3D) and sought to understand what role the nucleus plays as cells respond to extracellular cues, particularly mechanical cues. Few studies have directly measured the effect of nucleoskeletal disruption on cell behavior in response to mechanical properties of the environment. This is important because the nucleus is integral to cellular responses to force (Wang et al., 2009). In the current study, we have examined how the presence or absence of a nucleus affects cell polarization, cell migration, and mechanical signaling within cells.

Results

Generating cytoplasts

To address the physical role of the nucleus during cell migration, we removed the nucleus from mammalian cells, modifying an older approach (Wigler and Weinstein, 1975) to reproducibly generate high purity cytoplasts (cells without nuclei) from large populations ($\sim$2 $\times$ 10^7/gradient). We used both rat embryonic fibroblasts (REF52) and human umbilical vein endothelial cells (HUVECs) to generate cytoplasts. Cells were incubated in the presence of cytochalasin and centrifuged at high speed through a density gradient (Fig. 1 A). This resulted in formation of three distinct strata within the gradient. Fluorescence analysis of fractions from REF52 cells showed that fraction 1 contained mostly cellular debris, fraction 2 contained cytoplasts, and fraction 3 contained nucleoplasts (nuclei surrounded by cytosol and encased in plasma membrane; Fig. 1 B). Similar fractionation strata and composition were observed with HUVECs (Fig. S1 A). Based on morphological observations, enucleation appears to occur through repositioning of the nucleus through the cell body, leading to hyper-elongation of the cell parallel to the direction of the g-force vector (Fig. S1 B). Toward the tail end of the cytoplast (opposite end of nuclear exit), small fragments separate, generating the constituents of fraction 1. Enucleation occurs in the presence of g-force alone, but efficiency is increased with actomyosin destabilization (Fig. S1C). Enucleation of cells expressing nuclear localized-tdTomato led to

tdTomato fluorescence in cytoplasts with decreased presence in nucleoplasts (Fig. S1 D). This result is consistent with nuclear envelope rupture (Denais et al., 2016; Raab et al., 2016), which likely occurs during nuclear exit from the cell.

Cytometric profiling of stained fractions with a nuclear fluorescent dye showed 98.7 $\pm$ 0.6% purity for REF52 cytoplasts (Fig. 1 C) and 99.1 $\pm$ 0.8% purity for HUVEC cytoplasts (Fig. S1 E). Size analysis of REF52 fractions postenucleation revealed relative cell size order as intact > cytoplast > nucleoplast (Fig. S1 F). Volumetric measurements show cytoplasts are $\sim$64% the calculated volume of the cytoplasm of an intact cell (Fig. S1 G), suggesting that $\sim$36% is lost to the nucleoplast and debris fractions. Decreased levels of nuclear proteins within cytoplast fractions along with concomitant increases in levels in nucleoplast fractions were observed by blotting (Fig. 1 D). Similar cell-spreading rates (cytoplast K$_{1/2}$ = 20.6 $\pm$ 2.2 min; intact K$_{1/2}$ = 23.0 $\pm$ 2.0; P > 0.05), including typical radial morphology during spreading, were found between intact cells and cytoplasts (Fig. S1 H).

We analyzed cytoplasts for the presence of nuclear proteins, major organelles, and the cytoskeleton. Cytoplasts were devoid of nuclei and most nuclear-associated proteins (Figs. 1 E and S2 A); contained cytoskeletal networks for filamentous actin, vimentin, and microtubules; and formed vinculin-containing focal adhesions (Fig. 1 F). Cytoplasts retained endoplasmic reticulum, Golgi, mitochondria, and centrosomes (Fig. 1 G). Immunofluorescent staining of nucleoplasts revealed nuclear-associated proteins, organelles, and cytoskeletal systems (Fig. S2 B). We measured cytoplast survival with viability dyes and found REF52 cytoplasts to be stable for 48 h (Fig. 1 H). HUVEC cytoplasts had decreased viability compared with REF52 cells, showing a significant decrease at 6 h with loss of half the population at $\sim$18 h postenucleation (Fig. S2 C). We did not observe obvious decreases in protein levels for Src, nonmuscle myosin IIA, vinculin, and other proteins over 24 h in REF52 cytoplasts (Fig. S2 D). To reduce possible effects attributed to cytoplast deterioration over time, we used REF52 cytoplasts for most experiments, because they exhibited increased survival over HUVEC cytoplasts. These experiments were performed <27 h postenucleation, with most performed <19 h postenucleation. HUVEC cytoplasts were used for shorter experiments (<8 h), with 18-h experiments being the longest. Together, these data demonstrate the ability to generate a high quantity of cytoplasts with high purity.

The nucleus is not required for establishing anterior–posterior polarity

The positions of organelles, including the nucleus and centrosomes, are hallmarks of cell polarity. We assessed polarity establishment in the absence of the nucleus to understand whether the nucleus is necessary for proper localization of centrosomes and the Golgi apparatus. Micropatterns with bilateral, radial, and trilateral symmetries were used (crossbow, circle, and triangle, respectively; Fig. S3 A) to direct organelle positioning with respect to the cell centroid (Fig. S3 B), as performed by others (Théry et al., 2006). We report spatial information for organelle positioning relative to the cell centroid from y-coordinate values, as significant differences from the cell centroid were not found for x-coordinate values for all patterns tested (Fig. S3 C). Centrosomes, which normally position at the cell centroid, were indeed found near the cell centroid for REF52 intact cells and cytoplasts (Figs. 2 A and S3 D). The mean centrosome
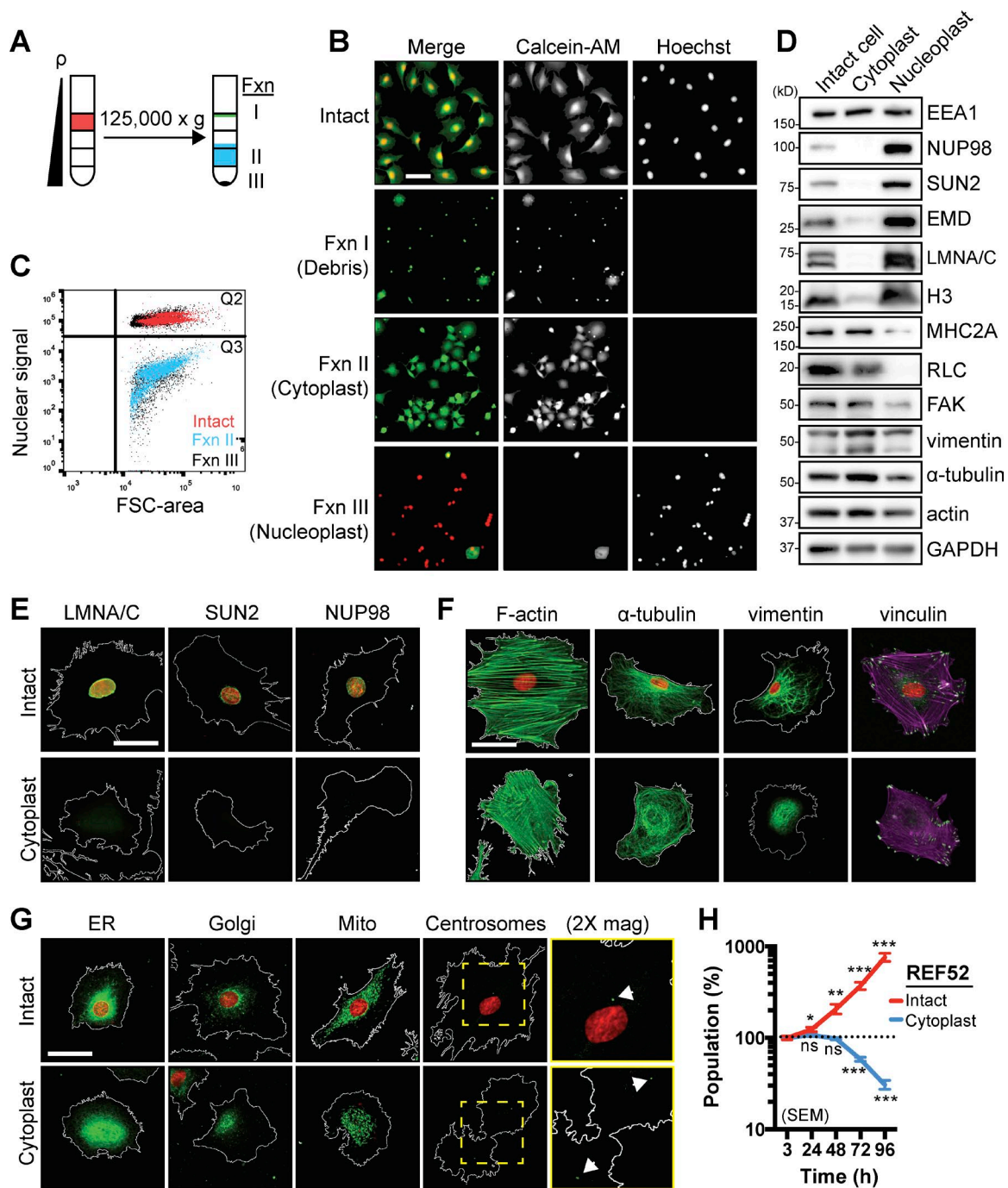
Figure 1. **Cytoplast generation and characterization. (A)** Illustration of enucleation procedure. **(B)** Fluorescence images of plated fractions 2 h after enucleation. **(C)** Cytometric profiles of stained populations with a fluorescent nuclear dye (Vybrant DyeCycle Green). Q2 is region containing positive nuclear staining. Q3 is negative for nuclear staining. **(D)** Western blots of intact cell, cytoplast, and nucleoplast fractions. **(E–G)** Immunofluorescent staining for nuclear proteins (E), cytoskeletal elements (F), and organelles (G). Arrowheads in G mark centrosomes. All nuclei are Hoechst stains and shown in red. Cell outlines are white. **(H)** Cell population as percentage of starting population over time shown as mean ± SEM ($n = 4$ experiments). Student's t test performed between successive time points for either intact cells or cytoplasts. ***, $P < 0.001$; **, $P < 0.01$; *, $P < 0.05$. Bars, 50 µm.

position for intact cells and cytoplasts on crossbows was -1.1 ± 0.4 and -1.2 ± 0.4 µm, respectively, from the cell centroid (Fig. 2 B). Similar to centrosomes, the Golgi positions between the nucleus and the cell leading edge; thus, we measured Golgi positioning on patterns. Consistent with centrosome localization, the Golgi was found near the cell centroid for intact cells and cytoplasts for all patterns tested (Figs. 2 C and S3 E), and the mean Golgi position did not differ between intact cells and

cytoplasts (Fig. 2 D). Next, we measured centrosome localization in HUVEC cytoplasts. HUVEC cytoplasts are smaller than REF52 cytoplasts and rarely occupied the full area of the circle micropattern (largest area of the patterns used), preventing us from considering this particular shape. Thus, we used triangle patterns instead. Centrosomes were positioned at the cell centroid for HUVEC intact cells and cytoplasts on crossbow and triangle micropatterns (Fig. 2, E and F). Together, these data
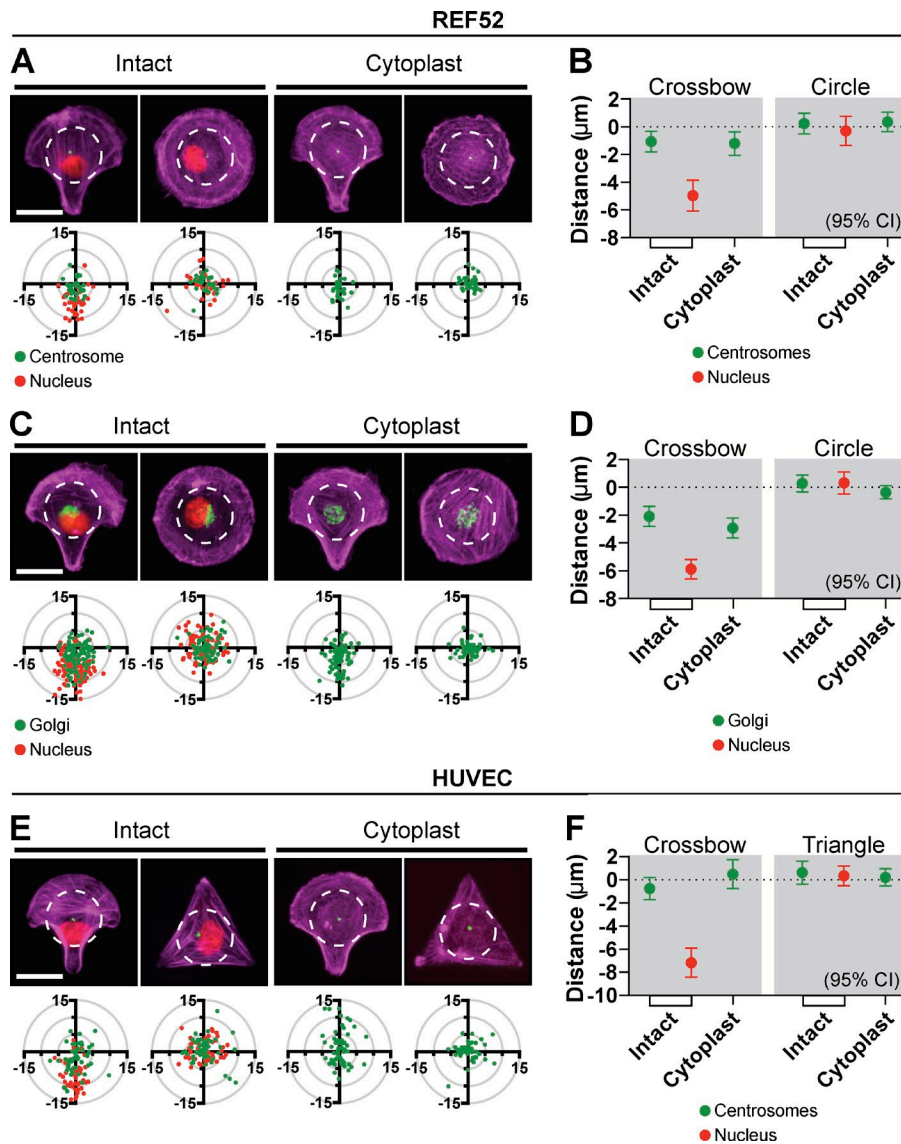
REF52

Figure 2. Cell polarity occurs in the absence of the nucleus. (A) Images and plots showing localization of centrosomes and nuclei from REF52 intact cells and cytoplasts plated on crossbow (intact cells, n = 39; cytoplasts, n = 35) and circle (intact cells, n = 34; cytoplasts, n = 31) patterns. **(B)** Mean y-coordinate distance ± 95% CI of centrosomes for REF52 intact cells and cytoplasts on crossbow and circle patterns. **(C)** Images and plots showing localization of Golgi and nuclei from REF52 cells plated on crossbow (intact cells, n = 100; cytoplasts, n = 86) and circle (intact cells, n = 78; cytoplasts, n = 57) patterns. **(D)** Mean y-coordinate distance ± 95% CI of Golgi for REF52 cells on crossbow and circle patterns. **(E)** Images and plots showing localization of centrosomes and nuclei from HUVEC intact cells and cytoplasts plated on crossbow (intact cells, n = 52; cytoplasts, n = 57) and triangle (intact cells, n = 50; cytoplasts, n = 49) patterns. **(F)** Mean y-coordinate distance ± 95% CI of centrosomes for HUVECs on crossbow and triangle patterns. All data are from at least three independent experiments. White dashed line circles in A, C, and E show a 30-µm-diameter region of interest. Bars, 25 µm.

demonstrate that normal cell polarization, as indicated by cell morphology and predicted organelle positioning, occurs independently of the nucleus.

The nucleus is not essential for random and directed 2D migration

Cell migration is intrinsically a polarity-driven process (Ridley et al., 2003). Thus, we analyzed 2D random migration in cytoplasts. We found REF52 and HUVEC cytoplasts were migratory, exhibiting anterior–posterior polarity, dynamic lamellipodial extension, and rear retraction (Figs. 3 A and S3 F and Videos 1 and 2). Intact cells displayed a biphasic migration velocity response on increasing fibronectin (FN) concentration, with velocity being slowest on both low (1 µg/ml) and high (≥100 µg/ml) concentrations (Fig. 3, B and C). Unexpectedly, cytoplasts from both REF52 cells and HUVECs did not reveal a biphasic response but instead showed increased migration velocity with increasing FN concentration. We measured the relative amount of FN on glass to determine if concentrations above 100 µg/ml were capable of binding and, as such, sensed by cells. Detectable increases in FN up to at least 400 µg/ml were measured, suggesting that 100 µg/ml is not saturating and that higher concentrations can

influence migration behavior (Fig. S3 G). We measured surface expression levels of β1 and β3 integrins in REF52 intact cells and cytoplasts to see whether reduced integrin levels, as a result of enucleation, might explain this response. Using flow cytometry and live-cell labeling with fluorescent-conjugated antibodies, we detected reduced levels of β1 and β3 integrins in cytoplasts as compared with intact cells (Fig. 3 D). However, when normalized to cell size (from flow cytometer forward-scatter metrics), the relative β1 and β3 integrin levels were not different between cytoplasts and intact cells. Furthermore, integrin localization was consistent with adhesion complexes. Lastly, we sought to gauge the effects of cytoplast deterioration on migration velocity, because this would influence migration efficiency over time. We found a decreased rate of −0.12 ± 0.02 µm/h over 24 h for REF52 cytoplasts (Fig. 3 E), demonstrating that cytoplast migration velocity is reduced over time.

Next, we examined directional migration in REF52 cytoplasts to determine what role the nucleus plays as cells respond to guidance cues. We measured directional migration via a microfluidic-based approach, as previously described (Wu et al., 2012). Migration was monitored in gradients of either PDGF (for chemotaxis) or surface-bound FN (for haptotaxis).
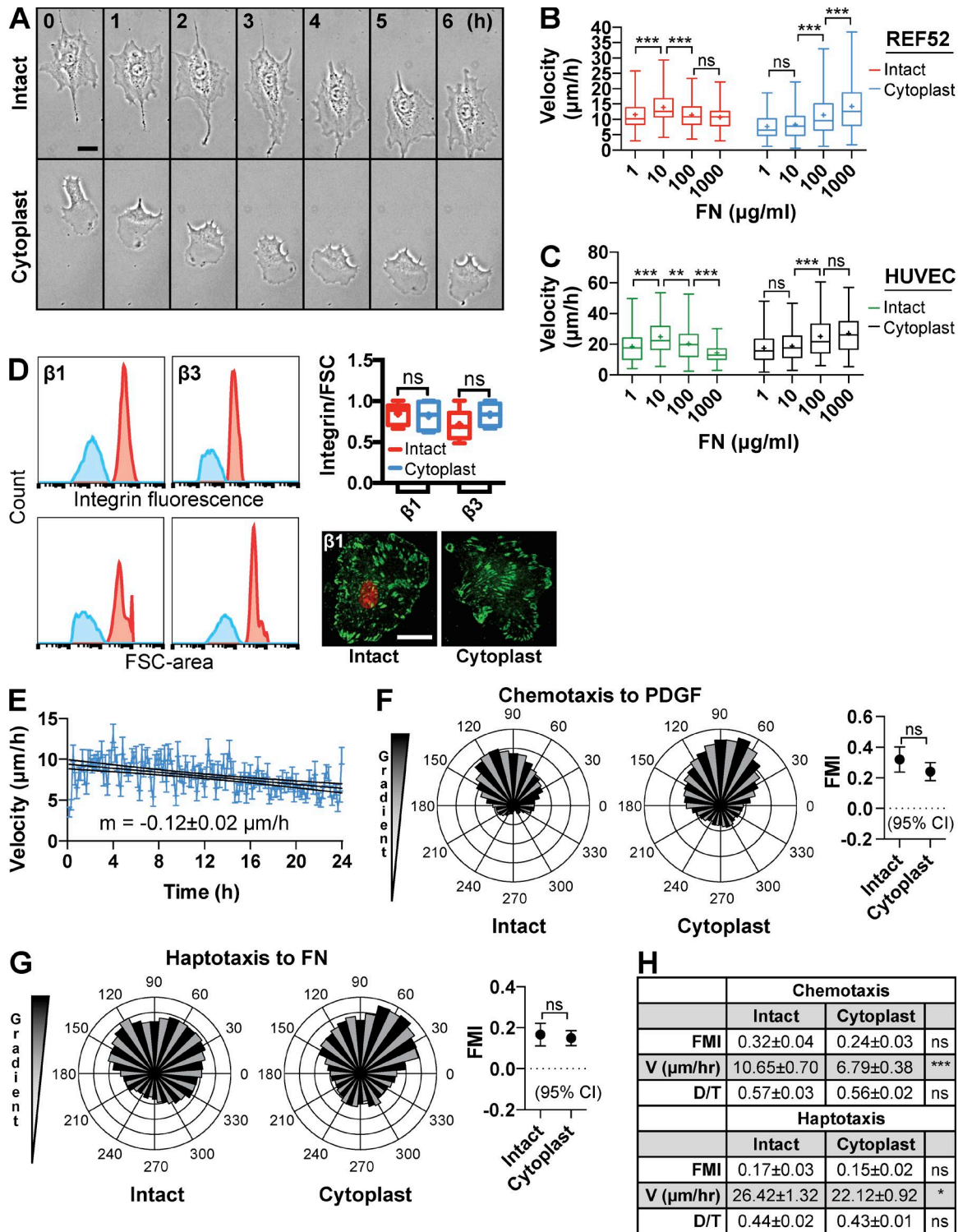
Figure 3. **Directed cell migration occurs in the absence of the nucleus. (A)** Stills of a REF52 intact cell and cytoplast migrating. **(B)** REF52 cell velocity on different concentrations of FN. *n* ≥ 100 cells per concentration for intact cells and cytoplasts. One-way ANOVA with Tukey's post-hoc test was performed. **(C)** HUVEC cell velocity on different concentrations of FN. *n* ≥ 90 cells per concentration for intact cells and cytoplasts. One-way ANOVA with Tukey's post-hoc test performed. **(D)** Histograms (left) from flow cytometry showing β integrin surface expression (top) and forward scatter area (FSC; bottom) for REF52 intact cells and cytoplasts. Graph (top right) of integrin/FSC for β integrins. Images of live-stained REF52 intact cell and cytoplast of equal spread area showing β1 surface staining. Cytometry data from two experiments are shown. **(E)** Mean cell velocity ± SEM over 24 h of cytoplast migration (*n* = 121 cells; data from two experiments). Linear regression fit to 24-h period ± 95% CI. **(F)** Rose plots (left) for intact cells (*n* = 169) and cytoplasts (*n* = 197) migrating in a PDGF gradient. Graph (right) showing mean FMI ± 95% CI. **(G)** Rose plots (left) for intact cells (*n* = 187) and cytoplasts (*n* = 199) migrating in a surface-bound FN gradient. Graph (right) showing mean FMI ± 95% CI. **(H)** Table showing FMI, cell velocity and persistence (displacement over total path length [D/T]) values from chemotaxis and haptotaxis experiments. Student's *t* tests were performed. Unless stated otherwise, all data are from at least three independent experiments. Bars, 25 µm. ***, P < 0.001; **, P < 0.01; *, P < 0.05.

Directional fidelity is shown as forward migration index (FMI), which describes the directional persistence of a cell toward (positive FMI) or away from (negative FMI) an extracellular cue. Cytoplasts showed positive chemotactic (Fig. 3 F) and haptotactic (Fig. 3 G) responses, similar to intact cells (Fig. 3 H). These data demonstrate that the nucleus is dispensable for directional migration in response to PDGF and FN.

The scratch-wound assay (herein referred to as the scratch assay) is widely used to measure collective and polarized migration. Proper nuclear repositioning in cells at the wound margin has been implicated in this migratory response (Gomes et al., 2005; Luxton and Gundersen, 2011). Thus, we assessed the physical necessity of the nucleus in this form of migration. Cytoplast monolayers from REF52 cells were mostly free of nuclei-containing cells (Fig. S4 A); however, purity decreased over time as any intact cells proliferated. We measured the density of nuclei at the end of all scratch experiments (∼16–20 h after scratch) and found nuclear densities of 15.6 ± 0.4 nuclei for intact cells and 1.3 ± 0.1 nuclei for cytoplasts in a 100-μm^2 area. At these densities, effects from intact cells within the cytoplast monolayer are unlikely to affect cytoplast-driven scratch closure. REF52 cytoplasts were capable of scratch closure, which occurred between 4 and 7 h for intact cells and 7 and 16 h for cytoplasts (Fig. 4 A and Video 3). The mean closure time for intact cells was 5.4 h. At this time, cytoplasts closed 80% of the scratch. On average, cytoplasts closed 95.6% of the scratch over 16 h. To reduce scratch closure effects driven by cell proliferation, we inhibited cell division with mitomycin C pretreatment (Fig. 4, B and D). The mean time for cytoplast scratch closure was unchanged from untreated; however, for intact cells, it increased from ∼5 to 8 h. Although the initial rates of scratch closure were similar for both intact cells and cytoplasts, total closure took longer for REF52 cytoplasts (Fig. S4 B). This difference may reflect the slight time-dependent decrease in migration velocity in cytoplasts. Despite this difference, the time to close half of the scratch ($t_{1/2}$) was not different between intact cells and cytoplasts for all treatments tested (Fig. 4 C). HUVEC cytoplasts were also capable of scratch closure (Fig. 4, E and F; and Video 4). A narrower scratch was used for these experiments (Fig. 4 F) to decrease the effects attributed to shorter viability. Similar to REF52 cells, HUVEC cytoplast monolayers were largely devoid of intact cells (Fig. S4 C) and were significantly slower than intact cells at scratch closure (Fig. S4 D). However, these cytoplasts showed nearly identical rates of closure for half of the scratch compared with intact cells (Fig. 4 G). Together, these data demonstrate that the nucleus is not necessary for closure in the scratch assay.

The nucleus is dispensable for migration in 1D, but not 3D, environments

Recent work has shown that the nucleus performs specialized physical functions during 3D migration (Petrie et al., 2014; Denais et al., 2016; Raab et al., 2016). We explored cytoplast migration in collagen gels of two different porosities to gauge cell migration efficacy in environments of different physical constraint and ligand density (Fig. 5 A). Collagen matrices were prepared with different gelation temperatures, producing loose reticular (LR) and highly reticular (HR) matrices, as described elsewhere (Doyle et al., 2015). Cytoplasts migrated slower than intact cells for both LR and HR matrices in both 2D (on top of the gel; Fig. 5 B) and 3D (inside the gel; Fig. 5 C and Video 5). Transitioning from 2D to 3D environments caused a decrease in

cell velocity for both intact cells and cytoplasts. Interestingly, cytoplast 3D velocity did not change between LR and HR matrices, whereas intact cell velocity decreased in HR matrices. Moreover, cytoplasts showed a less pronounced uniaxial morphology in 3D than intact cells (Fig. 5 D). Compared with intact cells, which showed a mean accumulated distance over 8 h of 91.4 ± 4.6 μm, cytoplasts were largely immotile, with a mean accumulated distance of 28.0 ± 1.2 μm (Fig. 5 E). The low velocity and low accumulated distance for REF52 cytoplasts were also observed for HUVEC cytoplasts (Fig. 5 F and Video 6). No difference in 3D cell velocity was measured between REF52 and HUVEC cytoplasts (3.0 ± 0.1 and 3.3 ± 0.3 μm/h, respectively; P > 0.05). This nonmigratory phenotype does not reflect the inability of cytoplasts to signal on collagen, because both phospho-FAK staining and phosphopaxillin staining were evident at focal adhesions when on collagen (Fig. S4 E). Additionally, cytoplasts were able to engage bundled collagen (Video 7) despite showing reduced contraction of collagen gels (Fig. S4 F). Cytoplasts were also able to degrade collagen (Fig. S4 G). We cannot rule out the inability of cytoplasts to polarize in 3D, because a reliable polarity marker for intact cells under these conditions was not found, thus preventing a controlled comparison. Collectively, these data are consistent with the role of the nucleus in facilitating migration in 3D, as previously reported (Petrie et al., 2014).

Next, we explored two mutually nonexclusive explanations for the impaired 3D migration of cytoplasts: (1) migration in 3D environments uniquely requires the physical presence of the nucleus (Petrie et al., 2017) or (2) the low-rigidity collagen matrices differentially affect cytoplasts versus intact cells. The first explanation is difficult to assess and might be addressed with nuclear addback experiments in 3D gels to rescue cytoplast migration in situ or the use of alternative 3D matrices that might confer migration to cytoplasts. Nuclear addback is technically difficult and was not attempted. The use of different matrix materials was not supported, because cytoplasts from primary human fibroblasts were shown to slowly migrate (∼4 μm/h) inside cell-derived matrices (Petrie et al., 2014), closely matching the low cell velocities we observed in collagen. Alternatively, the role of the nucleus in 3D migration could be determined with 1D migration being used as a surrogate for 3D, because these two forms of migration share several principles (Doyle et al., 2009). Thus, we turned to using micropatterned 1D lines (Fig. S4 H), where we found REF52 and HUVEC cytoplasts exhibited a uniaxial morphology and polarity, similar to intact cells. Contrary to our expectations, cytoplasts migrated in 1D (Fig. S4 I and Video 8) with velocities on 5-μm lines of 11.5 ± 0.6 μm/h for REF52 cells and 38.3 ± 1.5 μm/h for HUVECs (Fig. 5, G and H). Cytoplasts were also migratory on lines coated with either FN or collagen (Fig. S4 J). These data demonstrate that the nucleus is dispensable for migration in 1D, but not 3D, environments.

The nucleus regulates cell contractility and the sensitivity of the cell to mechanical cues

The ∼2-mg/ml collagen matrices used for our 3D work have a reported low stiffness, ranging between 0.2 and 0.6 kPa (Mason et al., 2013; Lang et al., 2015). Low matrix stiffness of ∼1 kPa has been reported for 3-mg/ml collagen matrices; this stiffness closely reflects the stiffness sensed at the cellular scale (Doyle et al., 2015). These stiffness values are far less
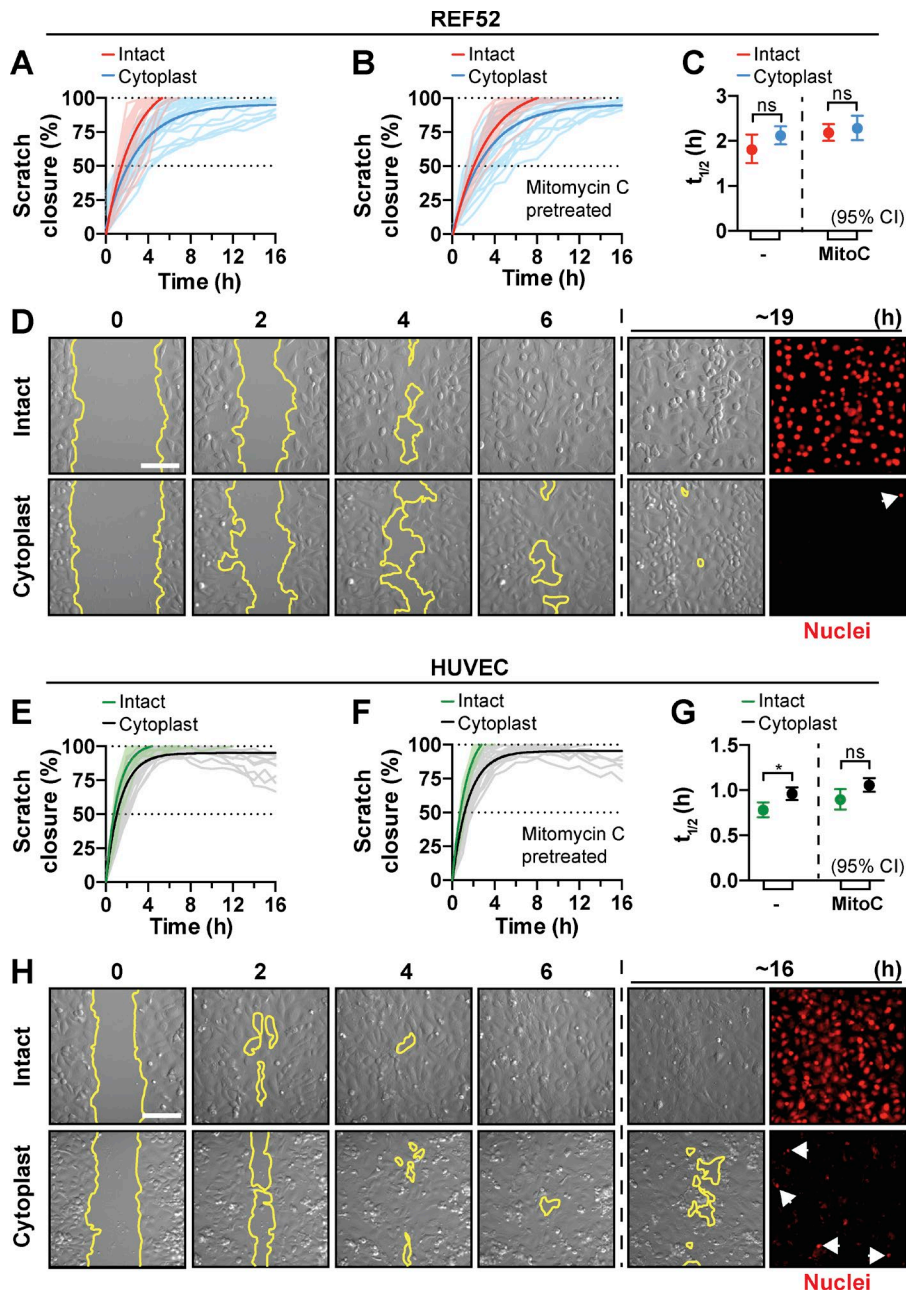
Figure 4. The nucleus is dispensable for directed migration in the scratch-wound assay. (A) Percent scratch-closure for intact cells (n = 27) and cytoplasts (n = 28). (B) Percent scratch-closure for mitomycin C–pretreated intact cells (n = 27) and cytoplasts (n = 22). (C) Mean time to close half of the scratch area ($t_{1/2}$ [h]) ± 95% CI. MitoC, mitomycin C. (D) Stills from scratch assay of REF52 intact cells (top) and cytoplasts (bottom) from mitomycin C treatment. Open scratch-area outlined in yellow. Arrowheads in D and H indicate nuclei. Data in A–D are from REF52 cells. (E) Percent scratch-closure for intact cells (n = 21) and cytoplasts (n = 28). (F) Percent scratch-closure for mitomycin C–pretreated intact cells (n = 30) and cytoplasts (n = 23). (G) Mean time to close half of the scratch area ($t_{1/2}$ [h]) ± 95%CI. (H) Stills from scratch assay of HUVEC intact cells (top) and cytoplasts (bottom) from mitomycin C treatment. Data in E–H are from HUVECs. Open scratch areas are outlined in yellow; arrowheads show nuclei. Note that dead cells also stained with nuclear dye, producing high apparent background. Bars, 100 µm. All scratch-closure graphs were fit with single-phase decay regressions. All data are from at least three independent experiments. Student's t tests were performed. ***, $P < 0.001$; **, $P < 0.01$; *, $P < 0.05$.

than commonly used plastic ($E > 10^6$ kPa) and glass ($E > 50 \times 10^6$ kPa) substrata for cells and may have an effect on cytoplast migration efficiency. Reliably altering the stiffness of 3D environments in a cell-compatible manner is not trivial, causing concomitant changes to ligand density and pore geometry. Consequently, we tested the effect of microenvironment stiffness on 2D migration by measuring migration in 2D on FN-coated substrata of known stiffness.

Using a range of hydrogels at 0.2, 0.5, 1, 8, 25, and 50 kPa and glass, we found intact cells and cytoplasts showed pronounced, biphasic responses in migration velocity with relation to substrata stiffness (Fig. 6 A). REF52 intact cells showed a peak migration velocity on 8-kPa substrata, whereas cytoplasts showed an unexpected peak migration velocity on 25-kPa substrata. When plotted together, a shift in peak of the biphasic response was evident, with the maximum cytoplast velocity significantly shifted toward stiffer substrata (Fig. 6 B). This

trend was not repeated upon inhibition of transcription or translation (Fig. S5 A). These data show cell migration velocity is dependent on substrate stiffness, which is a property observed in other cells (Peyton and Putnam, 2005; Plotnikov et al., 2012; Sunyer et al., 2016). Because mechanosensing depends upon both environmental forces and cell-generated forces (Janmey et al., 2009) and cell-generated forces are largely regulated by actomyosin-based contractility (Pelham and Wang, 1997; Pathak and Kumar, 2012; Raab et al., 2012), we surmised the shift in the optimum stiffness for migration could be a product of reduced whole-cell contractility and a reduction in mechanosensitive signaling on account of loss of the nucleus. For instance, if cell contractility is reduced, then a higher substratum rigidity would be necessary to activate mechanically sensitive pathways that regulate migration. To gain insight into this, we tested baseline mechanosensory responses in REF52 intact cells versus cytoplasts by subjecting them to identical conditions of biaxial
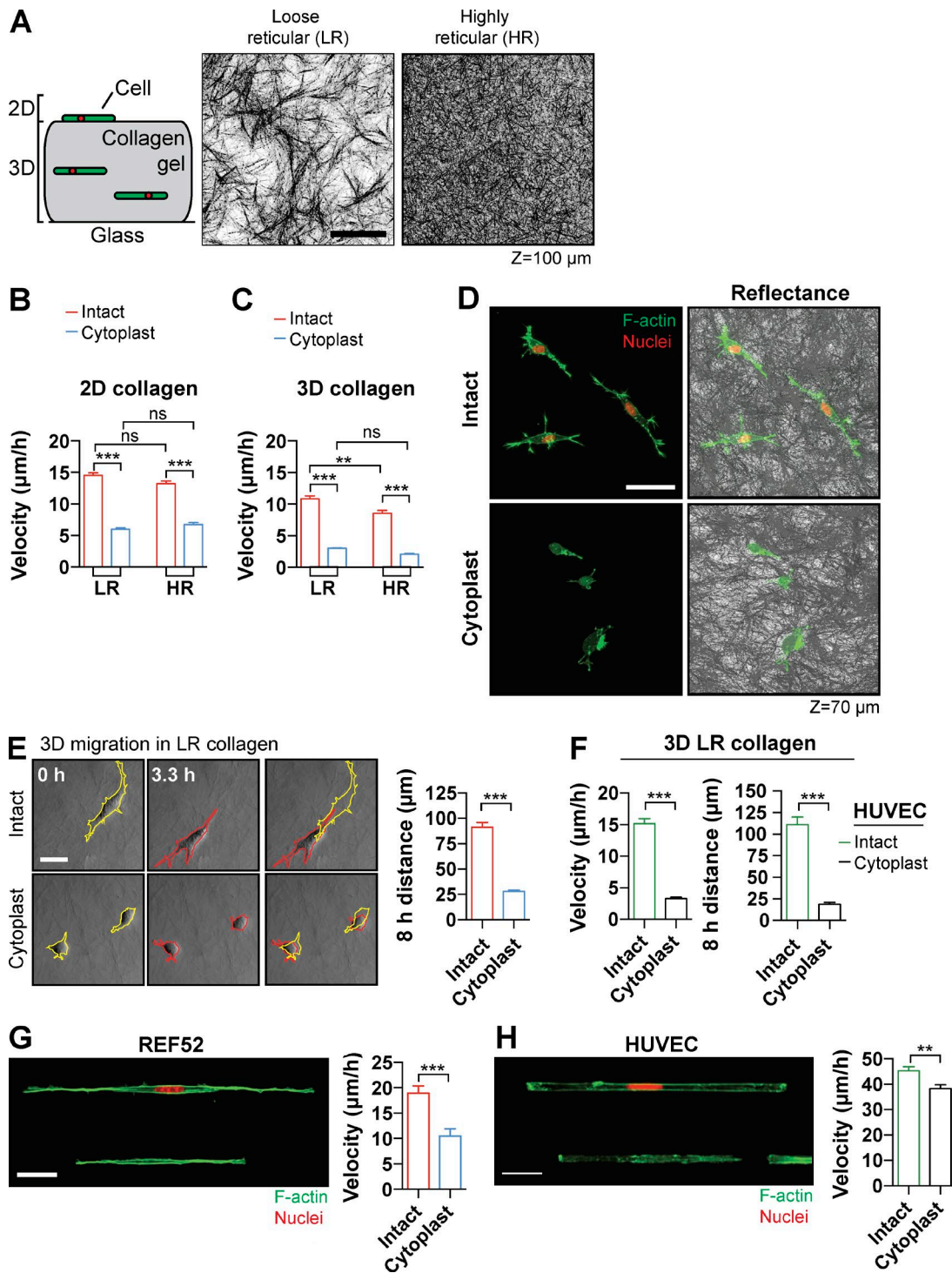
Figure 5. **The nucleus is dispensable for migration in 1D, but not 3D. (A)** Illustration of collagen matrix (left) for measuring 2D and 3D cell migration. Reflectance images (right) from 1.9 mg/ml self-assembled collagen polymerized to form LR or HR matrices, respectively. Bar, 50 µm. Image stack depth is 100 µm. **(B)** Mean 2D cell velocity ± SEM for REF52 cells on top of LR or HR matrices. Intact LR, n = 184; cytoplast LR, n = 169, intact HR, n = 62; cytoplast HR, n = 52. **(C)** Mean 3D REF52 cell velocity ± SEM for cells embedded in LR or HR matrices. Intact LR, n = 136; cytoplast LR, n = 111, intact HR, n = 50; cytoplast HR, n = 54. **(D)** Images of intact REF52 cells and cytoplasts in 3D LR collagen. Bar, 50 µm. Image stack depth is 70 µm. **(E)** Stills (left) of an intact cell (top) and cytoplasts (bottom) at 0 h (yellow outline) and 3.3 h (red outline). Graph (right) showing accumulated distance ± SEM from continuous 8 h of 3D migration for intact REF52 cells (n = 71) and cytoplasts (n = 64). **(F)** Graph (left) showing mean 3D cell velocity ± SEM for HUVECs embedded in LR matrix. Intact, n = 57; cytoplast, n = 64. Graph (right) showing accumulated distance ± SEM from continuous 8 h of 3D migration for intact cells (n = 35) and cytoplasts (n = 41). **(G)** Images of REF52 cells on 5-µm lines (left) and mean cell velocity ± SEM for 1D migration (right). Intact cells, n = 110; cytoplasts, n = 151. **(H)** Images of HUVECs on 5-µm lines (left) and mean cell velocity ± SEM for 1D migration (right). Intact cells, n = 96; cytoplasts, n = 108. Bars: (E, G, and H) 20 µm. All data are from at least three independent experiments. Student's t tests were performed. ***, P < 0.001; **, P < 0.01; *, P < 0.05.
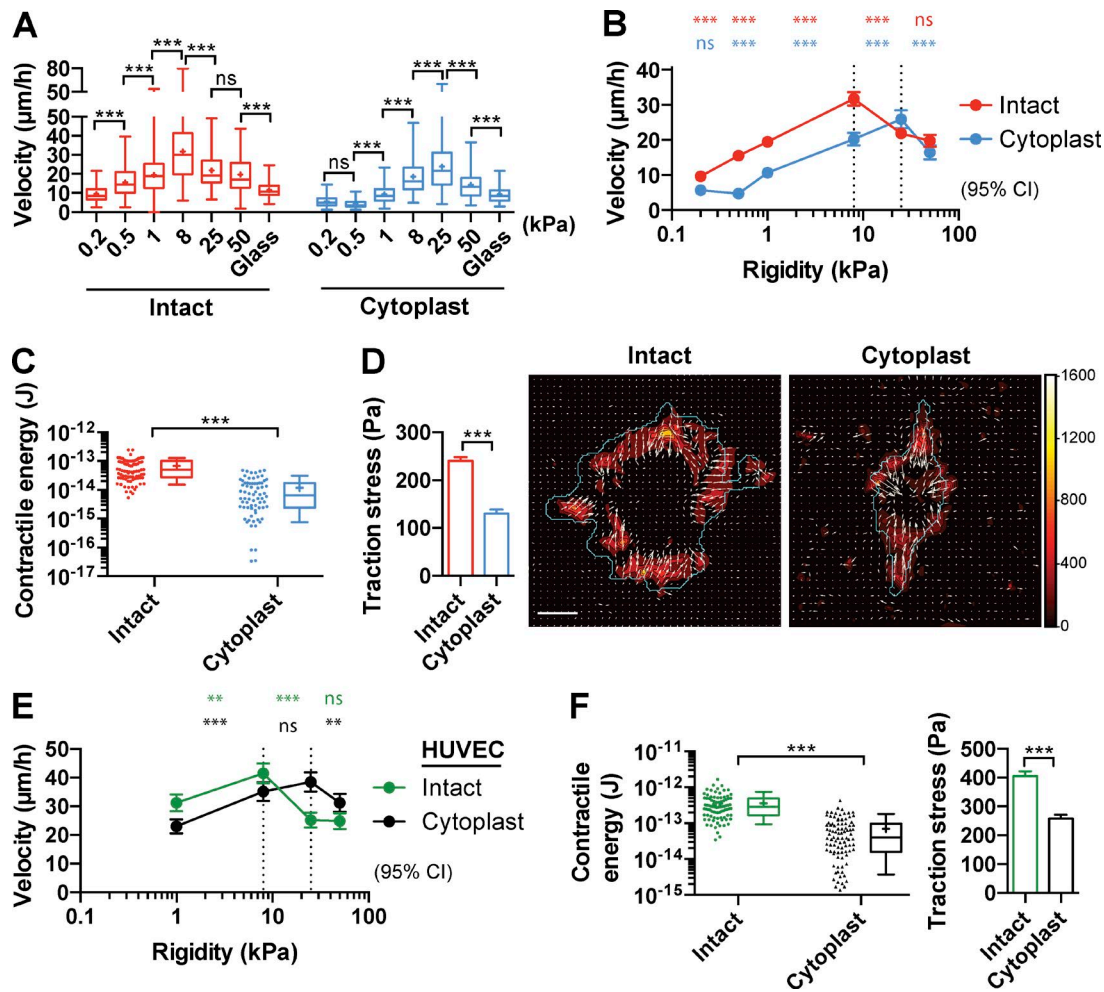
Figure 6. **The nucleus regulates cell contractility and migration in response to substratum rigidity. (A)** REF52 cell velocity on compliant substrata for intact cells ($n \geq 45$/stiffness) and cytoplasts ($n \geq 69$/stiffness). **(B)** Same data in A, showing overlay of cell velocity ± 95% CI on compliant substrata. **(C)** Contractile energy of REF52 intact cells ($n = 98$) and cytoplasts ($n = 72$). **(D)** Graph (left) showing mean traction stress ± SEM for REF52 intact cells and cytoplasts. Representative images (right) of traction stresses. Force vectors (arrows) and cell outlines (cyan) are shown. Bar, 20 µm. Scale is traction stress magnitude (in pascals). **(E)** Cell velocity ± 95% CI on compliant substrata for HUVEC intact cells ($n \geq 72$/stiffness) and cytoplasts ($n \geq 112$/stiffness). **(F)** Contractile energy graph (left) of HUVEC intact cells ($n = 89$) and cytoplasts ($n = 93$). Graph (right) showing mean traction stress ± SEM for HUVEC intact cells and cytoplasts. Dotted lines in B and E show 8 and 25 kPa. All data are from at least three independent experiments. Mann–Whitney U tests were performed for all traction force data. One-way ANOVA with Tukey's post-hoc test was performed between stepwise increases in stiffness for A, B, and E. Boxplots in C and F show 10th–90th percentiles. ***, $P < 0.001$; **, $P < 0.01$; *, $P < 0.05$.

cyclic strain. As previously reported, this results in activation of FAK through phosphorylation of Y397 (Li et al., 2001; Uzer et al., 2015). We found increased phospho-FAK levels after strain in both intact cells and cytoplasts. Interestingly, poststrain phospho-FAK levels were lower in cytoplasts than intact cells, suggesting that focal adhesion–based mechanotransduction is less sensitive to force cues in the absence of the nucleus (Fig. S5 B).

We used traction-force microscopy to measure the contractile energy (a whole-cell measure showing the mechanical effort used by the cell in substrate deformation [also known as strain energy]) and traction stress (a per-area-unit measure of the mechanical effort used by the cell in substrate deformation). We found that cytoplasts from REF52 cells had significantly reduced contractile energy and traction stress compared with intact cells (Fig. 6, C and D). This does not appear to be cell specific, because HUVEC cytoplasts also exhibited a similar shift in peak of the biphasic response toward more rigid substrata (Fig. 6 E) and showed decreased contractile energy and traction stress (Figs. 6 F and S5 C). These data, together with

the decreased collagen gel contraction by cytoplasts (Fig. S4 F), suggest that the nucleus regulates cell contractility and controls the sensitivity of the cell to mechanical cues.

The LINC complex and lamin A also regulate cell contractility and the sensitivity of the cell to mechanical cues

We sought to understand whether cell contractility and traction stress could be similarly regulated in intact cells with nuclear defects. The LINC complex mediates mechanical coupling between the cytoskeleton and nucleoskeleton via interactions between Nesprin and Sun proteins (Lombardi et al., 2011; Arsenovic et al., 2016). Thus, we codepleted Sun1/Sun2 (siSun1/Sun2) in REF52 cells (Fig. S5 D) to disrupt the LINC complex and subsequently decrease force transduction to the nucleus. Cells treated with a nontargeting siRNA (siCntl) showed a biphasic trend in cell migration velocity across different rigidities, with a peak cell velocity exhibited on 8-kPa substratum (Figs. 7 A and S5 B). In contrast, cells codepleted
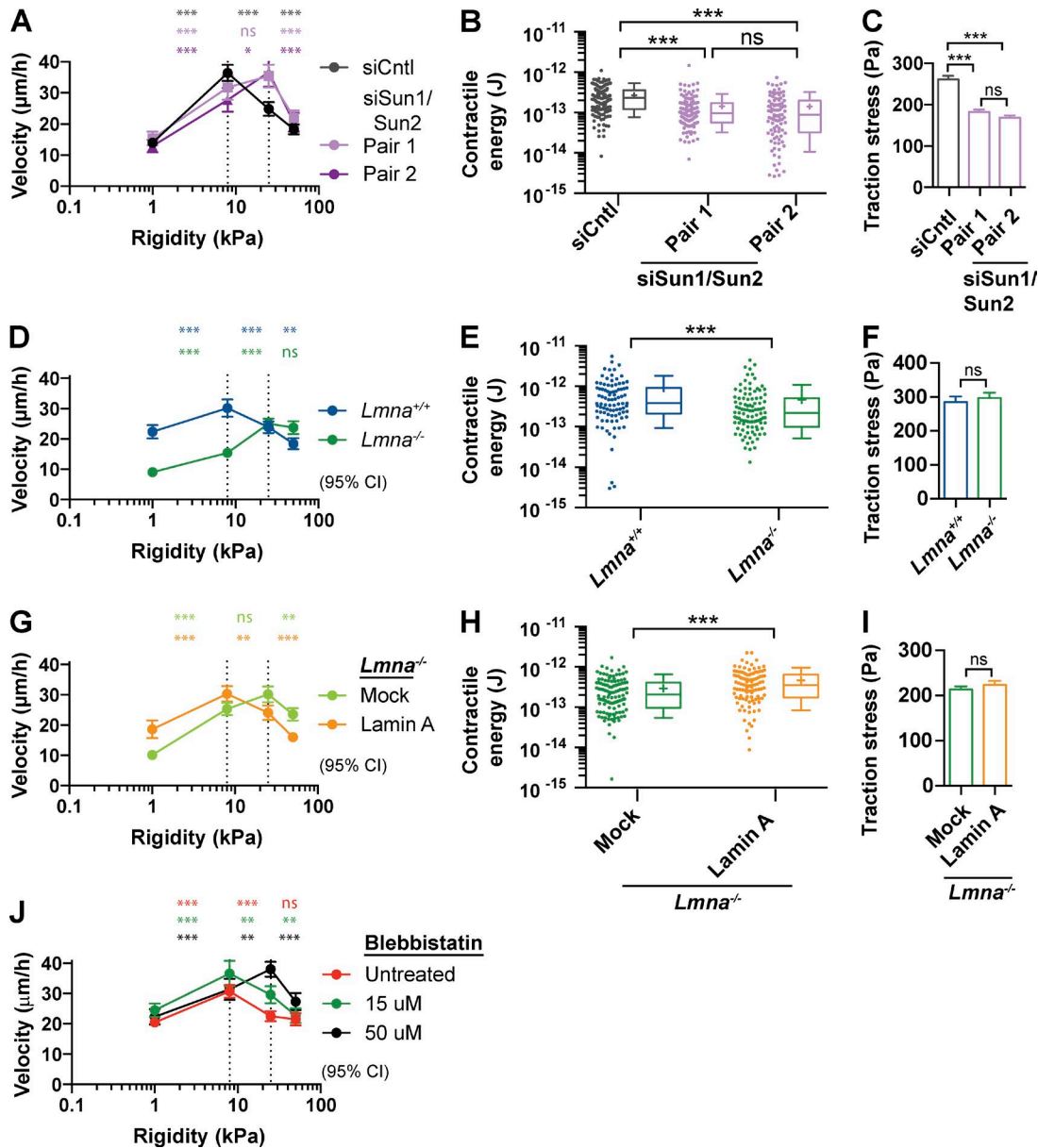
Figure 7. **The LINC complex and lamin A regulate cell contractility and migration in response to substratum rigidity.** **(A)** Cell velocity ± 95% CI on compliant substrata for REF52 cells treated with siCntl ($n \geq 118$/stiffness), siSun1/Sun2 siRNA pair 1 ($n \geq 71$/stiffness), and siSun1/Sun2 siRNA pair 2 ($n \geq 42$/stiffness). **(B)** Contractile energy of REF52 cells treated with siCntl ($n = 139$), siSun1/Sun2 siRNA pair 1 ($n = 117$), and siSun1/Sun2 siRNA pair 2 ($n = 97$). **(C)** Mean traction stress ± SEM for siCntl and siSun1/Sun2–treated REF52 cells. **(D)** Cell velocity ± 95% CI on compliant substrata for Lmna^{+/+} ($n \geq 79$/stiffness) and Lmna^{−/−} ($n \geq 113$/stiffness) cells. **(E)** Contractile energy of Lmna^{+/+} ($n = 90$) and Lmna^{−/−} ($n = 103$) cells. **(F)** Mean traction stress ± SEM for Lmna^{+/+} and Lmna^{−/−} cells. **(G)** Cell velocity ± 95% CI on compliant substrata for Lmna^{−/−} cells rescued with lamin A ($n \geq 69$/stiffness) or mock ($n \geq 67$/stiffness). **(H)** Contractile energy of Lmna^{−/−} cells rescued with lamin A ($n = 117$) or mock ($n = 106$). **(I)** Mean traction stress ± SEM for Lmna^{−/−} cells rescued with lamin A or mock. **(J)** Cell velocity ± 95% CI on compliant substrata for untreated intact REF52 cells ($n \geq 92$/stiffness) or in the presence of 15 µM ($n \geq 74$/stiffness) or 50 µM ($n \geq 60$/stiffness) bleb. Dotted lines in A, D, G, and J show 8 and 25 kPa. All data are from at least three independent experiments. One-way ANOVA with Tukey's post-hoc test was performed between stepwise increases in stiffness for A, D, G, and J. The Kruskal–Wallis test with Dunn's multiple comparisons was performed for B and C. The Mann–Whitney U test was performed for all other traction force data. Boxplots show 10th–90th percentiles. ***, $P < 0.001$; **, $P < 0.01$; *, $P < 0.05$.

of Sun1 and Sun2 showed a shift in peak of the biphasic response toward 8 and 25 kPa. Traction force analysis showed that siSun1/Sun2–treated cells have a lower contractile energy than controls (Fig. 7 B). Moreover, traction stress values were lower in siSun1/Sun2–treated cells than controls (Figs. 7 C and S5 E). These data support the role of the nucleus as a regulator of cell contractility to control the sensitivity of the cell to mechanical cues.

Lamin A/C is an important mechanosensitive nuclear protein (Swift et al., 2013) and is nonessential for LINC complex anchorage (Padmakumar et al., 2005; Crisp et al., 2006; Haque et al., 2006). We measured the mechanoresponses of cells bearing the total loss of this structural nuclear lamina protein. Using Lmna^{−/−} mouse embryonic fibroblasts (MEFs), we found a pronounced shift of the peak migration velocity toward 25- and 50-kPa substrata compared with a peak migration velocity at 8-kPa

substratum for Lmna$^{+/+}$ cells (Fig. 7 D). Consistent with this, traction-force measurements revealed a decreased contractile energy in Lmna$^{-/-}$ cells (Figs. 7 E and S5 F); however, traction stress was not different between Lmna$^{-/-}$ and Lmna$^{+/+}$ MEFs. Using Lmna$^{-/-}$ cells rescued with lamin A only (Fig. S5 G), the peak migration velocity on different rigidities was shifted toward less rigid substrata (peak at 8-kPa substratum) in rescued, but not mock rescued, cells (peak at 8- and 25-kPa substrata; Fig. 7 G). Remarkably, nearly complete restoration of contractile energy was measured in lamin A–rescued cells (Fig. 7 H). Similar to Lmna$^{-/-}$ and Lmna$^{+/+}$ MEFs, however, traction stress was not different between lamin A and mock-rescued Lmna$^{-/-}$ MEFs (Figs. 7 I and S5 H). These data demonstrate a similar nuclear-based modulation of cell migration and contractile energy to that observed in cytoplasts and cells bearing loss of the LINC complex. However, unlike enucleation or depletion of Sun1/Sun2 proteins, the presence of lamin A/C does not affect traction stress.

Lastly, we directly tested the role of cell contractility on regulating migration velocity on different rigidity substrata. Intact REF52 cells were treated with either 15 or 50 µM blebbistatin (bleb) to reduce actomyosin-based contractility while cell migration velocity on different rigidity substrata was measured. Consistent with our earlier measurements, cells showed a shift in peak of the biphasic migration velocity response from 8-kPa substratum, observed in untreated and 15 µM bleb–treated cells, to 25-kPa substratum with 50 µM bleb treatment (Fig. 7 J). The shift in peak migration that was measured upon nuclear loss, loss of connectivity between the cytoskeleton and nucleoskeleton, loss of lamin A/C, and inhibition of actomyosin-based contractility suggests a common pathway that regulates force transduction and cell migration response to environments of different rigidity. These data suggest that the nucleus can regulate the sensitivity of the cell to mechanical cues via modulation of whole cell contractility, a role consistent with the nucleus playing a role in an integrated molecular clutch.

Discussion

Cell biologists have investigated the physical role of the nucleus both in establishing cell polarity and in cell migration for many decades, with a more recent focus on its role in mechanotransduction. Based on our data using both fibroblasts and endothelial cells, we show that the nucleus is not necessary for establishing cell polarity or directional migration but is important for regulating the sensitivity of the cell to mechanical cues. Our data support a working model whereby the nucleus is a critical component of an integrated molecular clutch encompassing focal adhesions, actin stress fibers, and the nucleus.

The nucleus, cell polarity, and 2D cell migration

A relationship between the positions of the centrosome (microtubule-organizing center) and nucleus has long been recognized in many cells (Luxton and Gundersen, 2011). This relationship has been studied extensively, particularly in the context of cells in culture migrating into a scratch wound. For many migrating cells, there is an orientation of the centrosomal–nuclear axis such that the centrosome is located in front of the nucleus and the axis corresponds to the direction of migration. It has been shown that rearward nuclear movement reorients the position of the centrosome and that nuclear repositioning defines cell polarity (Gomes et al., 2005). These and other observations (Lee et al., 2007) have led to the view that the nucleus is critical for anterior–posterior cell polarity. Earlier work, however, suggested the opposite (Chambers and Fell, 1931; Goldstein et al., 1960; Goldman et al., 1973; Piel et al., 2000). We find that centrosome and Golgi localization occur with equal efficiency in the presence or absence of the nucleus, consistent with the notion that the nucleus is not strictly necessary for proper positioning of these organelles.

Similarly, we show that the nucleus is not essential for 2D migration under random and directed conditions. Although cytoplasts migrate more slowly on conventional FN concentrations (10 µg/ml) than control cells, similar migration velocities between cytoplasts and intact cells are found at higher FN concentrations. This suggests that the nucleus is not necessary for migration because changing FN density (which changes adhesion strength) can greatly modulate migration velocity. Given that the establishment of the centrosomal–nuclear axis has been implicated in directed migration, it is striking that cytoplast migration is little affected by the loss of the nucleus. Our directed migration data show cytoplasts chemotax and haptotax at efficiencies similar to intact cells. This indicates that the nucleus is not essential for sensing and responding to these extracellular cues or in establishing and maintaining the polarity required for directional migration. Furthermore, despite showing differences in total scratch closure time, our scratch assay data show similar rates of closure for half the scratch area between cytoplasts and intact cells. Several factors could potentially explain the total scratch closure time lag in cytoplasts, such as time-dependent cytoplast deterioration or decreased FN density from the scratch margin to the scratch center. However, our data indicate that a nucleus is not needed for the polarized positioning of the centrosome and Golgi or for directed cell migration.

Many studies have shown that disruption of proteins that associate the nucleus with the cytoskeleton, such as molecular motors, the LINC complex, and lamins, also cause concomitant defects in cell polarity, cell migration, and cytoskeletal organization (Nery et al., 2008; Roux et al., 2009; Chancellor et al., 2010; Fridolfsson and Starr, 2010; Luxton et al., 2010; Folker et al., 2011; Hale et al., 2011; Lombardi et al., 2011; Stewart et al., 2015). Our results do not contradict these earlier findings but rather indicate that whereas a misconnected or aberrantly positioned nucleus can perturb cell polarity and migration, the complete removal of the nucleus abrogates these defects. Though it is not known how an improperly positioned nucleus hinders cell polarity and migration in all contexts, it most likely involves the role of the nucleus in maintaining cytoskeletal organization and, through this, proper coordination of intra- and intercellular forces. The LINC complex directly mediates force transmission between the nucleus and cytoskeleton (Lombardi et al., 2011; Alam et al., 2015; Stewart et al., 2015; Arsenovic et al., 2016). Aberrant force transmission between the cytoskeleton and the nucleus could differentially affect force-sensitive signaling pathways that regulate polarity establishment and maintenance, as well as cell migration.

The nucleus and 3D cell migration

Although cytoplast migration on 2D surfaces was comparatively normal, it was greatly impaired in 3D collagen gels. At the outset of this study, we were uncertain what effect removing the nucleus would have on a cell's migration in 3D. This is

because the nucleus has been reported to both facilitate and impede migration efficiency in constrained spaces. For example, lobopodial migration is driven by a nuclear-piston mechanism that allows cells to move in 3D (Petrie et al., 2014). It is worth noting that this mechanism of migration does not explain our cytoplast 3D data because the nuclear-piston mechanism was shown in cell-derived matrices and does not operate in collagen matrices. Cytoplasts from that study, however, did show low migration velocity (∼4 µm/h) in cell-derived matrix, consistent with poor migration of cytoplasts in 3D environments.

In addition to the evidence that the nucleus positively contributes to 3D migration, other data suggest that in constrained spaces, the nucleus can limit 3D migration (Wolf et al., 2013). The nucleus can undergo high stress in these environments, leading to nuclear rupture and DNA damage (Denais et al., 2016). Increasing matrix pore size or increasing nuclear plasticity through decreasing levels of lamin A/C have been shown to increase cell migration in constrained spaces (Harada et al., 2014). One would predict that enucleation would increase migration velocity in 3D, based on evidence that a nucleus can restrain migration through narrow 3D matrices. However, we have found the opposite. Because cytoplasts can signal on collagen, exert force on collagen fibers, signal in response to mechanical load on collagen, and degrade and remodel matrix, these factors are unlikely to explain the impaired migration of cytoplasts in 3D.

Why do cytoplasts migrate so poorly in 3D environments? We considered two explanations: dimensionality and the low rigidity of the matrix used in our studies. We observed a general decrease in migration velocity upon changing between 2D and 3D collagen for both intact cells and cytoplasts. Because migration of cells along narrow lines of ECM (1D migration) is thought to be similar to 3D migration (Doyle et al., 2009), we examined how cytoplasts migrate on 1D FN-coated lines. Cytoplasts showed robust migration on these lines. However, these 1D matrix-coated lines were generated on rigid (glass) substrates, similar to the 2D random and directed migration studies described above. Consistent with this idea that rigidity may be critical, cytoplasts exhibit a relatively low migration velocity on the 2D top surface of 3D collagen gels. Ideally, we would have liked to test the role of rigidity in a 3D environment; however, this was technically challenging, because modifying the rigidity of collagen gels usually results either in concomitant changes in ligand density and/or changes in the porosity of the gel, making interpretation of any results ambiguous. Thus, we decided to tackle the rigidity question using 2D hydrogels of varying defined stiffness. Consistent with the idea that substrate stiffness largely accounts for differences between intact cell and cytoplast 3D motility, we observed a shift in the biphasic motility response, with cytoplasts requiring a stiffer substrate to achieve maximum cell velocity.

Impact of the nucleus on the integrated molecular clutch

The velocity of cell migration depends on both the density of the matrix molecules (e.g., FN) on the substrate and the rigidity of this surface. With both increasing matrix density and substratum rigidity, most cells demonstrate a biphasic migration velocity response (Lauffenburger and Horwitz, 1996; Peyton and Putnam, 2005; Pathak and Kumar, 2012). One of the striking results emerging out of our work is that the presence or absence of a nucleus (or connections to the nucleus) affects this response to matrix density and substrate rigidity. Removal of the nucleus shifted the peak velocity to higher matrix densities and higher substrate rigidities. For intact cells, the biphasic velocity response to increasing FN concentrations was generally interpreted as the result of too little adhesion being insufficient to generate optimal traction force, whereas too strong adhesion prevents detachment of adhesions, thereby retarding migration. However, agents that inhibit myosin activity or promote it were previously observed to shift the peak velocity to either faster or slower speeds depending on the FN concentration, indicating that the velocity profile could not be explained based on differences in adhesion strength alone (Gupton and Waterman-Storer, 2006). It was concluded that migration velocity reflects the interplay of many interdependent factors, including adhesion strength, myosin II activity, and actin dynamics (Gupton and Waterman-Storer, 2006). A large body of work has shown that migration velocity depends on nonmuscle myosin II and retrograde actin flow generating traction, as well as on "molecular clutches" (the sites of adhesion involving integrins, often clustered in focal adhesions) transmitting this traction to the substratum (Case and Waterman, 2015). Significantly, the behavior of the molecular clutch is affected by the rigidity of the substratum to which cells are adhering (Chan and Odde, 2008; Bangasser et al., 2017). The clutch properties reflect the number of adhesion molecules engaged, bond strength, and the types of bonds (catch bonds versus slip bonds).

Building on our enucleation results, we postulate that the LINC complex and nuclear lamina serve as a critical part of an extended and integrated molecular clutch that includes focal adhesions, contractile actin stress fibers, and the nucleus (Fig. 8). Actomyosin contractility regulates how cells sense and respond to force. The effect of enucleation on migration velocity was mimicked by inhibiting myosin II activity in intact cells with bleb. Also, consistent with cytoplasts having decreased contractility, they demonstrated reduced collagen gel contraction, decreased contractile energies, and decreased traction stresses. Similar results were obtained when we broke the cytoskeletal connections to the nucleus by disrupting the LINC complex through Sun1/Sun2 depletion. Again, this shifted the peak migration velocity to more rigid substrata and decreased contractile energy and traction stress. This suggests that nucleocytoskeletal connections regulate cell contractility and cell behavior in a manner similar to regulating actomyosin function. Because of the known structural connections between the nucleus and the actin cytoskeleton, a functional interdependence likely exists. Recent efforts have begun to dissect the signaling pathways regulating the LINC complex and actin cytoskeleton, revealing transcription-independent functions that involve regulation of RhoA activity (Thakar et al., 2017). Although our data support a role for nucleoskeletal connections in regulating cell contractility, it will be important in future studies to determine whether other activities such as actin retrograde flow rates and adhesion dynamics are also affected.

It is striking that although only a subset of actin filaments associate with the LINC complex (Khatau et al., 2009; Luxton et al., 2010), perturbing nucleocytoskeletal connections was sufficient to significantly decrease whole-cell contractility and alter mechanosensing. This suggests that LINC complex–associated actin filaments are particularly important in regulating whole-cell tension and cell migration. Consistent with this idea, distinct perinuclear focal adhesions have been reported to exist in several different cell lines, and LINC complex–associated
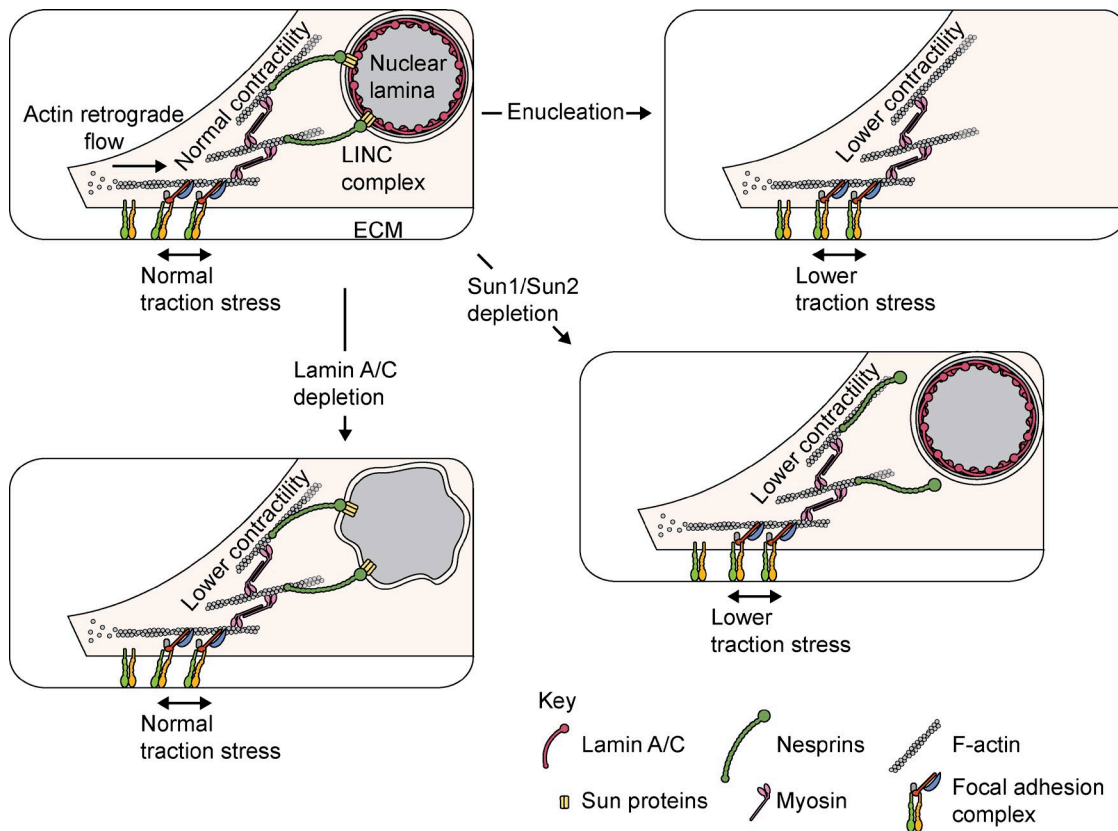
Figure 8. **The nucleus is an integral component of the molecular clutch.** Cartoon showing the nucleus as a structurally integrated, force-sensitive component of the molecular clutch model. The molecular clutch model proposes that ECM-bound integrins indirectly couple to actin retrograde flow and actomyosin contractility via force sensitive proteins (e.g., talin and vinculin) and, once engaged, are capable of bridging force between the extracellular environment and the cytoskeleton. An engaged molecular clutch can exert mechanical force on its environment through focal adhesions, giving rise to normal mechanical effort, as indicated by contractile energy and traction stress. The nucleus, though distal to the focal adhesion, is physically integrated with the cytoskeleton via the LINC complex. Enucleation, disruption of the LINC complex, and loss of lamin A/C caused a decrease in the contractile energy, whereas enucleation and disruption of the LINC complex caused a decrease in traction stress. Collectively, these nuclear defects manifest as lower migration velocity on physiologically normal substrata (~8 kPa) compared with controls. Upon increasing substrata rigidity (8–25 kPa), migration velocity was rescued, suggesting a greater force input was necessary to engage the molecular clutch.

actin filaments have been shown to terminate in focal adhesions that are distinct from the majority (Kim et al., 2012). According to this work, LINC complex–associated focal adhesions are mechanosensitive over a broad range of stiffness (5–500 kPa) as compared with conventional focal adhesions, which are mechanosensitive on only soft substrata (<5 kPa). Collectively, it is possible that nucleocytoskeletal disruption via enucleation or Sun1/Sun2 loss may selectively disrupt a distinct and crucial subset of focal adhesions that disproportionally affect the molecular clutch.

Mutations in nuclear lamins and LINC complex components affect cytoskeletal organization, cell migration, and physical properties of the cells. In particular, previous work with Lmna$^{-/-}$ cells has shown decreases in stress fiber organization, actin dynamics, focal adhesion area, RhoA activity, nuclear stiffness, mechanically induced nuclear signaling, and, more recently, contractility itself (Broers et al., 2004; Lammerding et al., 2006; Hale et al., 2008; Khatau et al., 2009; Ho et al., 2013; van Loosdregt et al., 2017). In our work, we have found that Lmna$^{-/-}$ cells also show a shift in the peak of their migration velocity to higher rigidity substrata. Consistent with these results, they also show decreased contractile energy, but unexpectedly, we did not detect a decrease in traction stress. The reason for this is currently unclear, but one possibility is that this reflects

the difference between a soft nucleus that is still attached via the LINC complex to the cytoskeleton as opposed to a disconnected nucleus (Fig. 8). Alternatively, Lmna$^{-/-}$ cells may be affecting other signaling pathways or experimental parameters, such as changes in the polarization of the traction forces, which in turn affect traction stress and cell migration (Jurado et al., 2005; Meili et al., 2010; Bastounis et al., 2014).

One important aspect of our integrated molecular clutch model (Fig. 8) is the bidirectional nature of force in the model. Force on the molecular clutch arises from retrograde actin flow, driving forward protrusion of the leading edge, and also from actomyosin contractility pulling the nucleus and rest of the cell body forward. Myosin-based contractility develops tension between the clutch and the nucleus because of the interconnections between the cytoskeleton and the nuclear envelope mediated by the LINC complex. The tension developed between these two structures (the adhesions and the nucleus) will be diminished externally by decreasing the rigidity of the substratum or internally by enucleation or disrupting the connections to the nucleus. The reduced tension transmitted to the clutch will, in turn, alter the cell's migratory response to both matrix rigidity and matrix density. Depleting lamin A, however, has an intermediate effect, because the nucleus is still connected to the actin cytoskeleton but is less rigid than a nucleus

in which lamin A is present (Haque et al., 2006; Lammerding et al., 2006). Our results highlight the continuing importance of understanding the cytoskeletal–nuclear interconnections and molecular details of the molecular clutch. During the past few years, much has been learned about how tension exerted on the clutch affects the properties and interactions of components mediating adhesion (Elosegui-Artola et al., 2016). Much still remains to be learned about these interactions and also how the signaling events generated by mechanical tension feeds back to impact cell behavior. Ultimately, this information should lead to a better understanding of how cells respond not only to the composition of their environment but also to its physical properties.

Materials and methods

Reagents and materials
Commercial antibodies used for Western blotting and immunohistochemistry were purchased from Cell Signaling Technology (rabbit anti-EEA1, rabbit anti-NUP98, rabbit anti-LMNA/C, mouse anti–histone H3, rabbit anti-MHC2A, rabbit anti-RLC [myosin regulatory light chain], rabbit anti-FAK, rabbit anti-FAK [Y397], rabbit anti-paxillin [Y118], rabbit anti-vinculin, rabbit anti-vimentin, rabbit anti-Src, rabbit anti-AMPKα, and rabbit anti-GAPDH), EMD Millipore (rabbit-anti-Sun1, rabbit anti-Sun2, and mouse anti-actin), Abcam (rabbit anti-emerin), Sigma-Aldrich (mouse anti–α-tubulin and mouse anti–γ-tubulin), BD (mouse anti-GM130), BioLegend (Alexa Fluor 488–conjugated anti–β1 and anti–β3 integrins), and Thermo Fisher Scientific (HRP-conjugated goat anti–mouse and goat anti–rabbit; Alexa Fluor 488, 568, and 633 goat anti–mouse and goat anti–rabbit). Phalloidin (Alexa Fluor 488, 568, 633), ER-Tracker Red (BODIPY), MitoTracker Green FM, CellTracker Green CMFDA, CellTracker Red CMTPX, calcein-AM, Hoechst 33342, Vybrant Dye-Cycle Green nuclear stain, and trypan blue were purchased from Thermo Fisher Scientific. Human FN used to conjugate to Cy5 was purchased from BD. Cy5 conjugation to FN was performed as previously described (Wu et al., 2012). FN used for all other experiments was purified from human plasma, as previously described (Engvall and Ruoslahti, 1977). Rat tail collagen type I was purchased from Advanced BioMatrix. Ficoll-400 was purchased from Fisher (BP525). Polyacrylamide hydrogels were purchased from Matrigen. Mitomycin C, GM6001, actinomycin D, cycloheximide, and SU6656 were purchased from Tocris. Cytochalasin B was purchased from Enzo Life Sciences. Blebbistatin was purchased from Sigma-Aldrich.

Cell culture, expression vectors, and RNAi experiments
REF52 cells were grown in high-glucose DMEM (Invitrogen) containing 10% FBS (Sigma-Aldrich) and 100 U/ml Pen-Strep (Invitrogen). Plasmid transfections were performed with Lipofectamine 2000 reagent (Invitrogen), based on manufacturer's protocol. Stable REF52 lines were generated by transfecting cells with specified constructs and sorting for fluorescence via successive rounds of flow cytometry. These lines include an NLS tdTomato chimera expressing line that was generated with the pQC-NLS-tdTomato construct (courtesy of C. Cepko's laboratory, Harvard Medical School, Boston, MA). A Golgi-EGFP–expressing line was used for all micropattern work and was generated with the pLL-5.5-GIX (Uetrecht and Bear, 2009) construct. This construct encodes a human β-1,4-galactosyltransferase-EGFP chimera. A centrin-EGFP–expressing line was generated with the p3XGFP-centrin construct. HUVECs were purchased from Lonza and cultured in EBM-2 endothelial growth basal medium (EBM-2). All lamin A/C MEF lines, including Lmna$^{+/+}$, Lmna$^{-/-}$, and Lmna$^{-/-}$ rescued with lamin A or mock rescued, were provided by J. Lammerding's laboratory (Cornell University, Ithaca, NY).

RNAi-mediated depletion of Sun1 and Sun2 was performed using siRNA duplexes purchased from Dharmacon. Two separate siRNA pairs were used for Sun1 and Sun2. These were siSun1/Sun2 pair 1: Sun1 (5′-GUAUAUACCAAGACGCCAU-3′), Sun2 (5′-GAGACUUACGAGACGAAGA-3′) and siSun1/Sun2 pair 2: Sun1 (5′-AUGUUGAAUUGGACGGCCA-3′), Sun2 (5′-GCUACAGUGAGGACCGUAU-3′). A nontargeting siRNA (5′-CGAACUCACUGGUCUGACC-3′) was used as a control. Transfection of 50-nM siRNA duplexes was performed with Mirus siQUEST reagent according to the manufacturer. Cells were used for experiments beginning at 48 h after transfection. Validation of RNAi-mediated depletion was monitored after each experiment via Western blot. Quantification of protein knockdown was measured using ImageJ.

Western blotting
Cells were lysed in either radioimmunoprecipitation assay lysis buffer (150 mM NaCl, 50 mM Tris-HCl, 1 mM EDTA, 0.24% sodium deoxycholate, and 1% Igepal, pH 7.5) or 2× Laemmli sample buffer (120 mM Tris-HCL, pH 6.8, 4% SDS, 20% glycerol, and 0.02% bromophenol blue). All lysis buffers contained 100 nM aprotinin, 50 µM leupeptin, 10 µM pepstatin A, and 50 mM sodium orthovanadate. Lysates were run on SDS-PAGE gels and transferred to polyvinylidene fluoride membranes (Immobilon-P; EMD Millipore). Membranes were blocked with either 5% (wt/vol) milk or bovine serum albumin for 1 h at ambient temperature before being incubated with primary antibodies overnight at 4°C. After primary antibody incubation, blots were washed and incubated with HRP-conjugated secondary antibody at ambient temperature for 1 h. Western blots were developed with SuperSignal West Pico or Femto Chemiluminescent Substrate (Thermo Fisher Scientific) and either scanned on a ChemiDoc MP System (Bio-Rad) or developed on film.

Cellular enucleation
Enucleation was performed essentially as described previously (Wigler and Weinstein, 1975), but with modifications. Of note, we observed variation in enucleation efficacy with Ficoll 400 from different commercial sources and even lot numbers. The greatest consistency was observed with Ficoll 400 from Fisher (BP525). Ficoll-400 was dissolved into a 50% (wt/vol) solution in sterile PBS (Ca^{2+}/Mg^{2+} free) through overnight rotation at ambient temperature. The stock was then diluted to 30% (vol/vol) with standard tissue culture media (DMEM containing 10% FBS and 100 U/ml Pen-Strep). The stock Ficoll solution was sterile filtered (0.4 µm) and stored at 4°C. The refractive index of the stock was measured on a refractometer. For the REF52 cell line and cells of similar volume/size (e.g., HUVEC, HeLa), the optimal refractive index of 1.373 produced good purity cytoplasts. Discontinuous iso-osmotic density gradients were poured from freshly prepared stocks of 30%, 20%, 18%, and 15% Ficoll-DMEM containing 10 µg/ml cytochalasin B (dissolved in 100% ethanol) and 0.2% DMSO. Next, 2 ml each of the 30%, 20%, and 18% solutions were layered into a 13.2-ml (14 × 89 mm; Beckman Coulter) cellulose nitrate centrifuge tube, with the greatest density starting at the bottom of the tube. Lastly, 1 ml of the 15% solution was added to the top. The remaining 15% solution was stored at 4°C. Prepared gradients were covered in Parafilm and left to equilibrate overnight in a tissue culture incubator. The SW41 Ti rotor buckets were incubated at 37°C overnight. The next morning, up to 2 × 10^7 cells per gradient were lifted from tissue culture dishes by either divalent-free PBS containing 5 mM EDTA or 0.05% trypsin-EDTA solution. Cells were pelleted, washed, and resuspended in 1 ml prewarmed 15% Ficoll-DMEM. Resuspended cells were then layered on the top

of the gradient. Lastly, the gradient was topped off with standard tissue culture media, filling the tube to the top, and then loaded into the prewarmed SW41 Ti rotor bucket and incubated in a tissue-culture incubator for 45 min. The gradient was then centrifuged in a Beckman Coulter Optima LE-80K ultracentrifuge at a relative centrifugal force max of 125,000 g (27,000 rpm) for 1 h at 30°C and stopped at minimal braking. Fractions were collected from the gradient and washed twice in PBS and twice in DMEM. Cell density and purity were measured on a Cellometer cell counter (Nexcelom) after staining fractions with the Vybrant DyeCycle Green nuclear stain.

Flow cytometry

Cells were suspended in PBS (Ca^{2+}/Mg^{2+} free) containing 0.5% FBS and 5 mM EDTA and stained with Vybrant DyeCycle Green stain at a final concentration of 5 µM for 15 min at 37°C. Samples were then filtered through a 30-µm filter (Sysmex; Partec CellTrics) and placed on ice. Stained populations were individually profiled in a Bio-Rad S3 flow cytometer. For population analyses, ~50,000 cells were profiled per sample. In addition to nuclear dye detection, cytoplasts were also identified from intact cells based on distinct side-scatter profiles. Periodically, this was used to assess cytoplast population purity. FlowJo (v10.1r5) software was used for graphic visualization of population distributions and extraction of statistical values. All fluorescence threshold values were designated based on unlabeled and labeled cells. Values reporting percent enucleation efficiency are based on seven independent enucleation runs.

Surface expression of integrins

Cell surface expression of β1 and β3 integrins was performed by staining adherent cells that had been seeded on 10 µg/ml FN for 3 h under tissue culture conditions. Cells were stained with Alexa Fluor 488–conjugated antibodies against β1 or β3 integrin (BioLegend) for 15 min in serum-containing medium in a tissue-culture incubator per the supplier's recommendation. Cells were trypsinized, pelleted, filtered through a 30-µm filter (Sysmex), and placed on ice before immediately profiling populations in a Bio-Rad S3 flow cytometer. Cytoplasts were initially profiled for purity using the Vybrant DyeCycle Green stain to ensure purity. Median integrin–Alexa 488 fluorescence values for each integrin were divided by the median forward scatter values for each respective population to provide a relative integrin/particle size ratio. Differences in relative integrin levels were not detected between intact cells and cytoplasts when either mean or geometric mean values for integrin–Alexa 488 fluorescence/forward scatter were measured. Values were measured from two independent experiments containing technical duplicates.

Microscopy and image analysis

Immunofluorescent and histochemical cell staining. Cells were fixed with 4% paraformaldehyde in Krebs S-buffer and permeabilized in 0.2% Triton X-100 in PBS for 10 min at room temperature. Cells were blocked for 30 min in PBS containing 5% BSA. Primary antibodies in PBS containing 1% BSA were stained overnight at 4°C followed by extensive washes in PBS. Dyes such as ER-Tracker Red (BODIPY), MitoTracker Green FM, and calcein-AM require living cells for staining and were used per the manufacturer's recommendation. Fluorescent dye–conjugated secondary antibodies were diluted to 1:1,000–1:3,000 in 1% BSA in PBS and applied for 1 h at ambient temperature followed by extensive washes in PBS. For nucleoplast stains, nucleoplasts were seeded onto 20 µg/ml FN–coated glass coverslips and, when appropriate, fixed after 30 min. Glass coverslips coated with poly-L-lysine resulted in higher retention of nucleoplasts. Nucleoplasts were permeabilized and stained as described above. Fluoromount-G (Electron

Microscopy Sciences) was used as the mounting medium for fixed cells on coverslips. Fluorescent images were acquired on either a Zeiss Axiovert 200M microscope using 20× or 40× objectives or on an Olympus FV1000 using a 40× objective.

Cell viability

Intact cells and cytoplast populations were stained with 1 µM calcein-AM (to label live cells), 0.2 µg/ml Hoescht 33342, and 0.04% (vol/vol) Trypan blue (to label dead cells) for 10 min in a tissue culture incubator. Dyes were washed out after staining, and images were acquired on an Axiovert 200M microscope with AxioVision software (Zeiss). Calcein-AM and Hoescht 33342 were imaged under fluorescent excitation/emission wavelengths suitable to each fluorophore, whereas trypan blue was imaged via transmitted light. Images were analyzed via automated particle counting with ImageJ software and verified by manual counting of randomly selected images from different time points. Stained populations were used for a single time point and were not restained for later time points. Viability data for intact cells and cytoplasts were derived from at least three independent experiments.

Cell outlines

Cell outlines were generated based on a masked phalloidin channel for all stains except for endoplasmic reticulum and mitochondria for the immunofluorescent and histochemical stains shown in Fig. 1. For endoplasmic reticulum and mitochondria images, cell outlines were manually drawn based on the transmitted light channel. To generate automatically detected outlines based on the phalloidin stain, a binary mask was generated with the phalloidin channel and the binary scale was inverted. Automated edge detection was performed using the "Find Edges" tool in ImageJ. The produced cell outline, designating the cell spread area of a cell, was preserved, whereas automatically outlined debris and background pixels were manually deleted so as to show only cell outlines. The resulting binary outlined channel was inverted, producing a white outline. This channel was then merged with the other stains for that cell. Cell outlines used for scratch assay experiments and matrix remodeling experiments were manually drawn using ImageJ and Adobe Illustrator.

Cell diameter and volume

Cell diameters of live REF52 intact cells and cytoplasts were measured using a Cellometer cell counter (Nexcelom). For volume measurements, cells were suspended in PBS (Ca^{2+}/Mg^{2+} free) and stained with calcein-AM and Hoechst 33342 dyes for 15 min at 37°C. Cells were seeded on glass-bottomed culture dishes that were coated with 0.5% BSA. Cells sedimented to the glass bottom and remained nonadherent. Using an Olympus FV1000 with a 40× objective, confocal fluorescent image stacks were generated for mixed populations of intact cells and cytoplasts. Image stacks were analyzed in ImageJ based on 3D projections of masked calcein-AM and Hoechst 33342 channels. Voxels were measured for each masked image.

Cell spreading

Cell spreading was performed in a 24-well plate coated with 10 µg/ml FN. Cells were lifted and washed twice in serum-free DMEM and seeded at equal number (2,000/well) in serum-free DMEM. The plate was placed in a tissue-culture incubator and fixed with 4% paraformaldehyde at 15-, 30-, 45-, 60-, 120-, and 180-min time points. Immediately after the addition of fixative to wells, Parafilm was used to completely cover fixative-containing wells. This approach prevented volatility-based effects caused by paraformaldehyde on neighboring wells. At the end of the experiment, all cells were permeabilized and stained with phalloidin and Hoechst 33342 dye. Wells were individually

imaged using an Axiovert 200M microscope using a 10× objective. Using ImageJ, images were masked for the phalloidin channel, segmented, and measured for area via automated measuring.

Micropatterning
Micropatterns for shapes (crossbow, circle, triangle) and lines (10 μm wide) were generated using a previously described UV-based photopatterning method (Azioune et al., 2010). (For micropatterning of 5-μm lines, see PNIPAM micropatterning.) In brief, a photomask was designed using AutoCAD (Autodesk) software. Micropatterns used were 50 × 50 μm in size and set 100 μm apart for crossbow, circle, and equilateral triangle shapes. Photolithography was commercially performed (Photo Sciences) on chrome-plated quartz with ±0.25 μm feature tolerance. Round 30-mm glass coverslips (Bioptechs) were cleaned with 70% ethanol and compressed air and plasma cleaned using a PDC-32G Harrick Plasma cleaner for 5 min. Cleaned coverslips were incubated overnight with 0.1 mg/ml poly-L-lysine–grafted polyethylene glycol (Surface Solutions Switzerland) in 15 mM Hepes, pH 7.5, by placing a 150-μl droplet of solution between a coverslip and Parafilm. Coverslips were then washed with deionized water and air dried. Before micropatterning, the photomask was cleaned using 70% ethanol and lint-free wipes (Texwipe). The photomask was placed chrome-side down from the UV source and irradiated in a UVO cleaner (Jelight) for 3 min. A 3-μl drop of deionized water was applied over micropattern region of photomask before loading the poly-L-lysine–grafted polyethylene glycol–coated surface of the coverslip on the photomask. The assembly was placed chrome-side up toward the UV source and irradiated for 3 min in the UVO cleaner. Coverslips were removed, briefly washed with PBS, and coated with 50 μg/ml FN or 250 μg/ml type-I rat tail collagen for 1 h at 37°C. FN-coated micropatterns were used immediately after preparation. Patterns were directly measured using a 40× objective on an Olympus FV1000 confocal microscope after coating with 50 μg/ml Cy5-conjugated FN.

PNIPAM micropatterning
Micropatterned poly(N-isopropylacrylamide) (PNIPAM) coverslips were used to produce 5-μm-wide lines and were produced as previously described (Mandal et al., 2012). In brief, PNIPAM brushes were grafted from glass coverslips and oxidized silicon wafers by surface-initiated atom transfer radical polymerization. N-isopropylacrylamide was purified by recrystallization in n-hexane. 3-Aminopropyl-triethoxysilane, triethylamine, $CuCl_2$, 1,1,7,7-pentamethyldiethylenetriamine, and 2-bromo-2-methylpropionyl bromide were used as received. All aqueous solutions were prepared in water. Glass and silicon substrates were cleaned in a 1 M sodium hydroxide aqueous solution for 15 min and rinsed with water. Samples were immersed for 1 min in an aqueous solution of 3-aminopropyl-triethoxysilane. After rinsing with water and drying in a nitrogen stream, samples were immersed for 1 min in a solution of 25 ml dichloromethane containing 1.2 ml triethylamine and 260 ml 2-bromo-2-methylpropionyl bromide, followed by rinsing with dichloromethane, ethanol, and water. This leads to surface immobilization of the atom transfer radical polymerization initiator. A solution of 1 g N-isopropylacrylamide, 150 ml 1,1,7,7-pentamethyldiethylenetriamine, and 20 ml water was prepared in a flask and bubbled with argon gas for 30 min before adding 25 mg CuCl. Initiator-grafted samples were immersed in this solution for a prescribed amount of time during which polymerization occurred and finally rinsed with pure water. Dry PNIPAM-bearing coverslips were placed in direct contact with a chromium quartz photomask (Toppan Photomasks). UV irradiation of the surfaces through the photomask was done in a custom-built device housing a set of four low-pressure mercury lamps (NIQ 60/35 XL longlife lamp, ~l–185 and 254 nm, quartz tube, 60 W; Heraeus

Noblelight GmbH). Samples were placed at a fixed distance of 9 cm from the UV tubes and irradiated for a prescribed duration between 5 and 10 min. PNIPAM micropatterns were coated with 50 μg/ml FN for all migration work. Line widths were directly measured using a 40× objective on an Olympus FV1000 confocal microscope after coating with 50 μg/ml Cy5–conjugated FN.

Polarity analysis
Cells were plated on micropatterned coverslips and allowed to adhere for 30 min before washing out nonadhered cells. Cells were allowed to spread for up to 3 h in growth media before fixation. REF52 stable lines expressing pLL-5.5-GIX or 3XGFP-centrin were used for Golgi and centrosome detection, respectively. HUVEC cells were stained for centrosomes with an antibody to γ-tubulin. Cells were stained with phalloidin and Hoechst 33342 dyes before mounting on large 75 × 38 × 0.96–1.06 (thick)-mm glass slides (Corning). Cells were imaged using a 20× objective on an Axiovert 200M widefield microscope with the 1.6× optovar in place. Only cells that fully occupied the full area of a pattern were analyzed. Image analysis was performed by measuring the center of mass/centroid for each channel of a single multichannel image, using ImageJ. For both crossbow and triangle patterns, images were rotated to register their orientation. For crossbow patterns, the "bow" portion of the crossbow was perpendicular to the vertical axis of the image frame. For triangle patterns, a vertex was positioned parallel to the vertical axis of the image frame. The resulting x,y-coordinate values for each channel (representing cell area, centrosome or Golgi, and nucleus) were compiled and normalized to the x,y coordinates of the centroid for the cell area. Single component analysis was performed with the normalized x or y coordinates for the centrosome, Golgi, and nucleus for each pattern.

Single-cell tracking
Glass-bottomed culture dishes (Mattek) or polyacrylamide hydrogels (Matrigen) were coated with 10 μg/ml FN (unless stated otherwise) at 37°C for 1 h. Cells were plated and allowed to spread for 3 h. Cells were imaged at 37°C with 5% CO_2 with a 20× objective under 0.5× magnification on an Olympus VivaView FL microscope or under 20× magnification on a Nikon Biostation IM microscope. For cytoplast work, nuclei were stained with the Vybrant DyeCycle Green nuclear stain at the end of experiments to avoid dye-induced toxicity. Single cell tracking was manually performed in ImageJ using the "Manual Tracking" plugin. Cells were tracked based on the approximate centroid location over time. Only single cells were tracked. Cells were no longer tracked after a collision event (with another cell or debris), migration out of the field of view, division, or death. Cells were not retracked if tracking was concluded for any of these reasons. Thus, cell tracks represent individual cells. To obtain velocity and persistence values, raw tracking data were analyzed with the "Chemotaxis Tool" plugin (Ibidi) in ImageJ.

Directional migration assays
Directional migration assays were performed as previously described (Wu et al., 2012). In brief, polydimethylsiloxane (PDMS; Sylgard 184; Dow Corning) microfluidic molds were cast from a custom silicon wafer. The microfluidic device was used to establish a gradient across a defined central chamber that was amenable to both cell migration and live-cell monitoring. For most experiments, intact cells and cytoplasts were plated together. Cells were allowed to spread for 2–3 h prior in the PDMS molds, and experiments were performed for 8–16 h under humidified 5% CO_2 at 37°C. Image acquisition was performed with MetaMorph imaging software (Molecular Devices), with images being acquired every 10 min from multiple stage positions. For chemotaxis, 10 μg/ml FN was used to coat the central chamber. A stable gradient

of PDGF in serum-free DMEM containing 10 µg/ml TRITC-dextran was continuously flowed across this chamber. The PDGF gradient was indirectly imaged based on TRITC-dextran signal. This signal was measured for slope before experiment. Cells were imaged with a 20× objective on an Olympus IX81 microscope. For experiments where intact cells and cytoplasts were coplated, cells were distinguished based on the presence of the nucleus, as determined by differential interference contrast illumination. For haptotaxis, a surface-bound gradient of Cy5-conjugated FN was generated across the central chamber of the PDMS microfluidic mold. The source FN concentration was 400–500 µg/ml. Cells were imaged with a 20× objective under 0.5× magnification on an Olympus VivaView FL microscope at 37°C with 5% CO_2. For experiments where intact cells and cytoplasts were coplated, cells were distinguished based on the presence of the nucleus, as determined by staining at the end of the experiment with Vybrant DyeCycle Green nuclear stain. For all direct migration, single-cell tracking was manually performed in ImageJ using the Manual Tracking plugin. To obtain FMI, persistence, and velocity values, raw tracking data were analyzed with the "Chemotaxis Tool" plugin (Ibidi) in ImageJ. Rose plots were generated using the "secplot" script for MATLAB (http://www.mathworks.com/matlabcentral/fileexchange/14174-secplot).

Scratch assay

Glass-bottomed culture dishes (Mattek) were coated with 10 µg/ml FN for 1 h at 37°C. Cells were densely plated for 2–3 h to establish monolayers. Monolayers were rinsed to remove nonadhered and piled-up cells. For mitomycin C pretreatment, adhered cells were pretreated with 5 µg/ml mitomycin C for 2 h before enucleation. Mitomycin C–treated cells were then plated for 2–3 h before generating a scratch. For experiments with REF52 cells, scratches were made using a P200 pipet tip at a ~45° angle, resulting in a ~200-µm-wide scratch. For HUV ECs, scratches were made using a gel loading pipet tip at a ~45° angle, resulting in a ~100-µm-wide scratch. Cells were imaged every 10 min for 16 h with a 20× objective under 0.5× magnification on an Olympus VivaView FL microscope. Nuclei were stained with the Vybrant DyeCycle Green nuclear stain at the end of all experiments. Nuclear density was measured for both intact cells and cytoplasts at the end of experiments via sampling three random regions per nuclear image with a 100 µm × 100 µm–square region. These values were then averaged and reported per scratch assay run. Scratch closure was measured for each hour over a 16-h experiment by manually outlining the open cleft area using ImageJ. Scratch closure rates were measured from three or four fields of view per dish. Closure rates were quantified relative to the starting area of the cleft (from $t = 0$). All data were collected from at least three independent experiments.

Collagen matrices

Collagen matrices were formed as described previously (Rommerswinkel et al., 2014). In brief, 50 µl of 10× MEM (Gibco) and 27 µl of 7.5% sodium bicarbonate (Thermo Fisher) were added to 375 µl of 3.3 mg/ml rat tail type-I collagen (Advanced BioMatrix). From this mixture, 115 µl was added to 50 µl of DMEM-10% FBS containing 10^4 cells. The resulting collagen concentration is 1.9 mg/ml. Next, 150 µl of the combined collagen-cell mixture was loaded onto the glass portion of a glass-bottom culture dish (Mattek) and allowed to gel at either 21°C or 37°C for LR or HR matrices, respectively. For 2D migration studies, 50 µl collagen-cell mixture was loaded onto the glass portion of the dish to enable feasible working distance for microscopy. For 21°C gelling, dishes were inverted for the first 10–15 min to avoid cell sedimentation before placing right-side up until complete gelling occurred. Dishes were gently flooded with culture medium after 30 min for 37°C gels and 1 h for 21°C gels, and left to

equilibrate for 2–3 h. Cells were imaged every 10 min with a 20× objective under 0.5× magnification on an Olympus VivaView FL microscope. Nuclei were stained with the Vybrant DyeCycle Green nuclear stain at the end of experiments.

Gelatin degradation

Matrix metalloproteinase activity was indirectly assessed via the invadopodia assay, essentially as described elsewhere (Chan et al., 2014). In brief, acid-washed coverslips were coated with 100 µg/ml poly-L-lysine in PBS for 20 min, washed in PBS, incubated with 0.5% glutaraldehyde for 15 min, and then washed in PBS. Coverslips were incubated in a 2 mg/ml final concentration of a 4:1 mixture of porcine gelatin/FITC-conjugated porcine gelatin (Thermo Fisher Scientific) for 1 h at 37°C. Coverslips were quenched with 1% fatty-acid–free BSA for 30 min at 37°C. Cells were incubated on gelatin-coated coverslips for 24 h. As a control, matrix metalloproteinase was inhibited by incubating cells in 10 µM GM6001 over the 24-h incubation. Gelatin degradation was quantified from images acquired using an Axiovert 200M microscope with a 40× objective. Images were analyzed using ImageJ.

Collagen contractility assay

Collagen gels were generated by adding 500 µl of 10× MEM (Gibco), 200 µl culture medium, and 270 µl of 7.5% sodium bicarbonate (Thermo Fisher Scientific) to 3.75 ml of 3.3 mg/ml rat tail type-I collagen (Advanced BioMatrix). From this mixture, 765 µl was added to 1.235 ml culture medium containing 10^6 cells. In a 24-well plate, 400 µl of this mix was added to each well and allowed to gel at 37°C with periodic shaking every 15 min to prevent cell sedimentation. After 1 h, medium was gently added to each well. A P20 pipet tip was used to separate the gel from the well. Samples were placed in an incubator for 24 h before plates were imaged using a desktop scanner (Canon), and images were analyzed using ImageJ. Percent contraction was calculated for each well by measuring the area of the collagen gel and normalizing this value to the area of collagen gels containing no cells. Data were derived from two independent experiments containing technical triplicates.

Biaxial cyclic strain assay

The biaxial strain was performed essentially as described elsewhere (Uzer et al., 2015). In brief, REF52 intact cells and cytoplasts were plated at a density of 30,000 cell/cm^2 per well in six-well BioFlex collagen-I coated plates (BF-3001C; Flexcell). After plating for either 3 or 18 h, cells were subjected to dynamic uniform biaxial cyclic strain at 5% magnitude at 10 cpm for 20 min using the Flexcell FX 5000 under conditions of 37°C and 5% CO_2. Control plates were handled the same but without strain application. Immediately after strain, whole-cell lysates were prepared and probed for phospho-FAK, total FAK, and GAP DH via Western blot analysis. Blots were analyzed using ImageJ. Data were derived from three independent experiments.

Traction-force microscopy

Traction-force work was performed on 8-kPa hydrogels containing 1-µm-diameter fluorescent (580/605–nm) beads (Matrigen). Hydrogels were coated with 20 µg/ml FN before seeding with cells in normal tissue culture conditions. Cells were allowed to spread overnight, and were imaged under 40× magnification using an Olympus VivaView FL microscope. CellTracker Green was added to spread cells (1:5,000), and individual, single cells were randomly selected for imaging. Imaged cells were not in close proximity to other cells so as to eliminate neighbor effects. Cells were imaged using DIC and CellTracker Green fluorescence. Beads were imaged under TRITC excitation/emission wavelengths. Traction force calculations were performed as described previously (Mandal et al., 2014). The contractile energy strictly defines

the total energy Ec transferred from the cell to the elastic distortion of the substrate and is given by

$$Ec = \frac{1}{2}\int \vec{T}(\vec{r}) \cdot \vec{u}(\vec{r}) dxdy,$$

where T(r) is the traction stress applied by the cell and u(r) is the displacement of a point on the elastic substrate. A Fourier transform traction cytometry algorithm with zero-order regularization was used to calculate cellular traction forces from the measured substrate displacements. Substrate displacements were determined from the images of fluorescent beads embedded inside the gel, first in the presence and then in the absence of adherent cells. To release adhered cells, 1% Triton X-100 prewarmed to 37°C was added to dishes to 0.5% Triton X-100 final volume. After correction for experimental drift, the displacement field was determined in two steps: (1) particle image velocimetry on subimages followed by (2) tracking of individual beads. The final displacement field was obtained by linear interpolation on a regular grid with 0.84-µm spacing. Force reconstruction was conducted under the assumption that the substrate was a linear elastic half-space. All traction force data were derived from at least three independent experiments.

Statistical analysis

All statistical analyses were performed using Prism (GraphPad Software). A linear-regression fit was performed for plot showing cytoplast migration velocity over a 24-h period. Single-phase decay, nonlinear regression analyses were performed for all other line-fit plots. Error bars on bar graphs represent the SEM. Error bars on graphs reporting cell spreading rates, organelle polarity, forward migration indices, scratch assay closure rates, and migration velocity-rigidity rates represent the 95% confidence intervals (CIs). Error bars on boxplots represent the 10th–90th percentiles for data showing 1D line widths and for data showing contractile energy values. An outlier test using the robust regression and outlier removal method with the false discovery rate value (Q) at 1% was performed for data reporting cell diameters and cell velocity. With the exception of the traction force data, statistical significance was measured for all data with the assumption that populations fit a Gaussian distribution. Gaussian-based tests performed were the two-tailed Student's t test and the one-way ANOVA with Tukey's post-hoc test. Nonparametric tests performed were the Mann–Whitney U test and the Kruskal–Wallis test with Dunn's multiple comparisons. One-way ANOVA with Newman–Keuls post-hoc test was performed for biaxial strain experiments.

Online supplemental material

Fig. S1 shows information relevant to cytoplast generation and characterization and is supplemental to Fig. 1. Fig. S2 shows information relevant to cytoplast generation and characterization and is supplemental to Fig. 1. Fig. S3 shows information relevant to the cell polarity analyses on micropatterns and migration data on FN-coated surfaces and is supplemental to Figs. 2 and 3. Fig. S4 shows information relevant to cytoplast migration in the scratch assay, cytoplast responses on collagen surfaces, and 1D migration data and is supplemental to Figs. 4 and 5. Fig. S5 shows information relevant to the mechanoresponse of intact cells and cytoplasts, as well as cells bearing LINC complex disruption and lamin A/C loss, and is supplemental to Figs. 6 and 7. Video 1 shows random migration of a REF52 intact cell and cytoplast and is related to Fig. 3 A. Video 2 shows random migration of a HUVEC intact cell and cytoplast and is related to Fig. S3 F. Video 3 shows collective migration of REF52 intact cells and cytoplasts in a scratch assay and is related to Fig. 4 D. Video 4 shows collective migration of HUVEC intact cells and cytoplasts in a scratch assay and is related to Fig. 4 H. Video 5 shows 3D migration of REF52 intact cell and cytoplasts in LR collagen and

is related to Fig. 5 C. Video 6 shows 3D migration of HUVEC intact cells and a cytoplast in LR collagen and is related to Fig. 5 F. Video 7 shows a REF52 cytoplast engaging and displacing collagen fibers and is related to Figs. 5 C and S4 F. Video 8 shows 1D migration of REF52 intact cells and a cytoplast and is related to Figs. 5 G and S4 I.

References

Alam, S.G., D. Lovett, D.I. Kim, K.J. Roux, R.B. Dickinson, and T.P. Lele. 2015. The nucleus is an intracellular propagator of tensile forces in NIH 3T3 fibroblasts. *J. Cell Sci.* 128:1901–1911. https://doi.org/10.1242/jcs.161703

Arsenovic, P.T., I. Ramachandran, K. Bathula, R. Zhu, J.D. Narang, N.A. Noll, C.A. Lemmon, G.G. Gundersen, and D.E. Conway. 2016. Nesprin-2G, a Component of the Nuclear LINC Complex, Is Subject to Myosin-Dependent Tension. *Biophys. J.* 110:34–43. https://doi.org/10.1016/j.bpj.2015.11.014

Azioune, A., N. Carpi, Q. Tseng, M. Théry, and M. Piel. 2010. Protein micropatterns: A direct printing protocol using deep UVs. *Methods Cell Biol.* 97:133–146. https://doi.org/10.1016/S0091-679X(10)97008-8

Bangasser, B.L., G.A. Shamsan, C.E. Chan, K.N. Opoku, E. Tüzel, B.W. Schlichtmann, J.A. Kasim, B.J. Fuller, B.R. McCullough, S.S. Rosenfeld, and D.J. Odde. 2017. Shifting the optimal stiffness for cell migration. *Nat. Commun.* 8:15313. https://doi.org/10.1038/ncomms15313

Bastounis, E., R. Meili, B. Álvarez-González, J. Francois, J.C. del Álamo, R.A. Firtel, and J.C. Lasheras. 2014. Both contractile axial and lateral traction force dynamics drive amoeboid cell motility. *J. Cell Biol.* 204:1045–1061. https://doi.org/10.1083/jcb.201307106

Borrego-Pinto, J., T. Jegou, D.S. Osorio, F. Auradé, M. Gorjánácz, B. Koch, I.W. Mattaj, and E.R. Gomes. 2012. Samp1 is a component of TAN lines and is required for nuclear movement. *J. Cell Sci.* 125:1099–1105. https://doi.org/10.1242/jcs.087049

Broers, J.L.V., E.A. Peeters, H.J. Kuijpers, J. Endert, C.V. Bouten, C.W. Oomens, F.P. Baaijens, and F.C. Ramaekers. 2004. Decreased mechanical stiffness in LMNA-/- cells is caused by defective nucleo-cytoskeletal integrity: implications for the development of laminopathies. *Hum. Mol. Genet.* 13:2567–2580. https://doi.org/10.1093/hmg/ddh295

Case, L.B., and C.M. Waterman. 2015. Integration of actin dynamics and cell adhesion by a three-dimensional, mechanosensitive molecular clutch. *Nat. Cell Biol.* 17:955–963.

Chambers, R., and H.B. Fell. 1931. Micro-Operations on Cells in Tissue Cultures. *Proc. R. Soc. Lond., B.* 109:380–403. https://doi.org/10.1098/rspb.1931.0090

Chan, C.E., and D.J. Odde. 2008. Traction dynamics of filopodia on compliant substrates. *Science.* 322:1687–1691.

Chan, K.T., S.B. Asokan, S.J. King, T. Bo, E.S. Dubose, W. Liu, M.E. Berginski, J.M. Simon, I.J. Davis, S.M. Gomez, et al. 2014. LKB1 loss in melanoma disrupts directional migration toward extracellular matrix cues. *J. Cell Biol.* 207:299–315. https://doi.org/10.1083/jcb.201404067

Chancellor, T.J., J. Lee, C.K. Thodeti, and T. Lele. 2010. Actomyosin tension exerted on the nucleus through nesprin-1 connections influences endothelial cell adhesion, migration, and cyclic strain-induced reorientation. *Biophys. J.* 99:115–123. https://doi.org/10.1016/j.bpj.2010.04.011

Crisp, M., Q. Liu, K. Roux, J.B. Rattner, C. Shanahan, B. Burke, P.D. Stahl, and D. Hodzic. 2006. Coupling of the nucleus and cytoplasm: role of the LINC complex. *J. Cell Biol.* 172:41–53. https://doi.org/10.1083/jcb.200509124

Denais, C.M., R.M. Gilbert, P. Isermann, A.L. McGregor, M. te Lindert, B. Weigelin, P.M. Davidson, P. Friedl, K. Wolf, and J. Lammerding. 2016. Nuclear envelope rupture and repair during cancer cell migration. *Science.* 352:353–358.

Doyle, A.D., F.W. Wang, K. Matsumoto, and K.M. Yamada. 2009. One-dimensional topography underlies three-dimensional fibrillar cell migration. *J. Cell Biol.* 184:481–490. https://doi.org/10.1083/jcb.200810041

Doyle, A.D., N. Carvajal, A. Jin, K. Matsumoto, and K.M. Yamada. 2015. Local 3D matrix microenvironment regulates cell migration through spatiotemporal dynamics of contractility-dependent adhesions. *Nat. Commun.* 6:8720. https://doi.org/10.1038/ncomms9720

DuFort, C.C., M.J. Paszek, and V.M. Weaver. 2011. Balancing forces: architectural control of mechanotransduction. *Nat. Rev. Mol. Cell Biol.* 12:308–319. https://doi.org/10.1038/nrm3112

Elosegui-Artola, A., R. Oria, Y. Chen, A. Kosmalska, C. Pérez-González, N. Castro, C. Zhu, X. Trepat, and P. Roca-Cusachs. 2016. Mechanical regulation of a molecular clutch defines force transmission and transduction in response to matrix rigidity. *Nat. Cell Biol.* 18:540–548. https://doi.org/10.1038/ncb3336

Elosegui-Artola, A., I. Andreu, A.E.M. Beedle, A. Lezamiz, M. Uroz, A.J. Kosmalska, R. Oria, J.Z. Kechagia, P. Rico-Lastres, A.L. Le Roux, et al. 2017. Force triggers YAP nuclear entry by regulating transport across nuclear pores. *Cell.* 171:1397–1410.e14. https://doi.org/10.1016/j.cell.2017.10.008

Engvall, E., and E. Ruoslahti. 1977. Binding of soluble form of fibroblast surface protein, fibronectin, to collagen. *Int. J. Cancer.* 20:1–5. https://doi.org/10.1002/ijc.2910200102

Euteneuer, U., and M. Schliwa. 1984. Persistent, directional motility of cells and cytoplasmic fragments in the absence of microtubules. *Nature.* 310:58–61. https://doi.org/10.1038/310058a0

Euteneuer, U., and M. Schliwa. 1992. Mechanism of centrosome positioning during the wound response in BSC-1 cells. *J. Cell Biol.* 116:1157–1166. https://doi.org/10.1083/jcb.116.5.1157

Folker, E.S., C. Östlund, G.W.G. Luxton, H.J. Worman, and G.G. Gundersen. 2011. Lamin A variants that cause striated muscle disease are defective in anchoring transmembrane actin-associated nuclear lines for nuclear movement. *Proc. Natl. Acad. Sci. USA.* 108:131–136.

Fridolfsson, H.N., and D.A. Starr. 2010. Kinesin-1 and dynein at the nuclear envelope mediate the bidirectional migrations of nuclei. *J. Cell Biol.* 191:115–128. https://doi.org/10.1083/jcb.201004118

Goldman, R.D., R. Pollack, and N.H. Hopkins. 1973. Preservation of normal behavior by enucleated cells in culture. *Proc. Natl. Acad. Sci. USA.* 70:750–754. https://doi.org/10.1073/pnas.70.3.750

Goldstein, L., R. Cailleau, and T.T. Crocker. 1960. Nuclear-cytoplasmic relationship in human cells in tissue culture. *Exp. Cell Res.* 19:332–342. https://doi.org/10.1016/0014-4827(60)90012-4

Gomes, E.R., S. Jani, and G.G. Gundersen. 2005. Nuclear movement regulated by Cdc42, MRCK, myosin, and actin flow establishes MTOC polarization in migrating cells. *Cell.* 121:451–463. https://doi.org/10.1016/j.cell.2005.02.022

Graham, DM; Burridge. 2016. Mechanotransduction and nuclear function. *Current Opinion in Cell Biology.* 40:98–105. https://doi.org/10.1016/j.ceb.2016.03.006

Guilluy, C., L.D. Osborne, L. Van Landeghem, L. Sharek, R. Superfine, R. Garcia-Mata, and K. Burridge. 2014. Isolated nuclei adapt to force and reveal a mechanotransduction pathway in the nucleus. *Nat. Cell Biol.* 16:376–381. https://doi.org/10.1038/ncb2927

Gundersen, G.G., and H.J. Worman. 2013. Nuclear positioning. *Cell.* 152:1376–1389. https://doi.org/10.1016/j.cell.2013.02.031

Gupton, S.L., and C.M. Waterman-Storer. 2006. Spatiotemporal feedback between actomyosin and focal-adhesion systems optimizes rapid cell migration. *Cell.* 125:1361–1374. https://doi.org/10.1016/j.cell.2006.05.029

Hale, C.M., A.L. Shrestha, S.B. Khatau, P.J. Stewart-Hutchinson, L. Hernandez, C.L. Stewart, D. Hodzic, and D. Wirtz. 2008. Dysfunctional connections between the nucleus and the actin and microtubule networks in laminopathic models. *Biophys. J.* 95:5462–5475. https://doi.org/10.1529/biophysj.108.139428

Hale, C.M., W.-C. Chen, S.B. Khatau, B.R. Daniels, J.S.H. Lee, and D. Wirtz. 2011. SMRT analysis of MTOC and nuclear positioning reveals the role of EB1 and LIC1 in single-cell polarization. *J. Cell Sci.* 124:4267–4285. https://doi.org/10.1242/jcs.091231

Haque, F., D.J. Lloyd, D.T. Smallwood, C.L. Dent, C.M. Shanahan, A.M. Fry, R.C. Trembath, and S. Shackleton. 2006. SUN1 interacts with nuclear lamin A and cytoplasmic nesprins to provide a physical connection between the nuclear lamina and the cytoskeleton. *Mol. Cell. Biol.* 26:3738–3751. https://doi.org/10.1128/MCB.26.10.3738-3751.2006

Harada, T., J. Swift, J. Irianto, J.W. Shin, K.R. Spinler, A. Athirasala, R. Diegmiller, P.C.D.P. Dingal, I.L. Ivanovska, and D.E. Discher. 2014. Nuclear lamin stiffness is a barrier to 3D migration, but softness can limit survival. *J. Cell Biol.* 204:669–682. https://doi.org/10.1083/jcb.201308029

Ho, C.Y., D.E. Jaalouk, M.K. Vartiainen, and J. Lammerding. 2013. Lamin A/C and emerin regulate MKL1-SRF activity by modulating actin dynamics. *Nature.* 497:507–511. https://doi.org/10.1038/nature12105

Jaalouk, D.E., and J. Lammerding. 2009. Mechanotransduction gone awry. *Nat. Rev. Mol. Cell Biol.* 10:63–73. https://doi.org/10.1038/nrm2597

Janmey, P.A., J.P. Winer, M.E. Murray, and Q. Wen. 2009. The hard life of soft cells. *Cell Motil. Cytoskeleton.* 66:597–605. https://doi.org/10.1002/cm.20382

Jurado, C., J.R. Haserick, and J. Lee. 2005. Slipping or gripping? Fluorescent speckle microscopy in fish keratocytes reveals two different mechanisms for generating a retrograde flow of actin. *Mol. Biol. Cell.* 16:507–518. https://doi.org/10.1091/mbc.E04-10-0860

Khatau, S.B., C.M. Hale, P.J. Stewart-Hutchinson, M.S. Patel, C.L. Stewart, P.C. Searson, D. Hodzic, and D. Wirtz. 2009. A perinuclear actin cap regulates nuclear shape. *Proc. Natl. Acad. Sci. USA.* 106:19017–19022. https://doi.org/10.1073/pnas.0908686106

Kim, D.-H., S.B. Khatau, Y. Feng, S. Walcott, S.X. Sun, G.D. Longmore, and D. Wirtz. 2012. Actin cap associated focal adhesions and their distinct role in cellular mechanosensing. *Sci. Rep.* 2:555. https://doi.org/10.1038/srep00555

Lammerding, J., L.G. Fong, J.Y. Ji, K. Reue, C.L. Stewart, S.G. Young, and R.T. Lee. 2006. Lamins A and C but not lamin B1 regulate nuclear mechanics. *J. Biol. Chem.* 281:25768–25780. https://doi.org/10.1074/jbc.M513511200

Lang, N.R., K. Skodzek, S. Hurst, A. Mainka, J. Steinwachs, J. Schneider, K.E. Aifantis, and B. Fabry. 2015. Biphasic response of cell invasion to matrix stiffness in three-dimensional biopolymer networks. *Acta Biomater.* 13:61–67. https://doi.org/10.1016/j.actbio.2014.11.003

Lauffenburger, D.A., and A.F. Horwitz. 1996. Cell migration: a physically integrated molecular process. *Cell.* 84:359–369. https://doi.org/10.1016/S0092-8674(00)81280-5

Lee, J.S.H., C.M. Hale, P. Panorchan, S.B. Khatau, J.P. George, Y. Tseng, C.L. Stewart, D. Hodzic, and D. Wirtz. 2007. Nuclear lamin A/C deficiency induces defects in cell mechanics, polarization, and migration. *Biophys. J.* 93:2542–2552. https://doi.org/10.1529/biophysj.106.102426

Li, W., A. Duzgun, B.E. Sumpio, and M.D. Basson. 2001. Integrin and FAK-mediated MAPK activation is required for cyclic strain mitogenic effects in Caco-2 cells. *Am. J. Physiol. Gastrointest. Liver Physiol.* 280:G75–G87.

Lombardi, M.L., D.E. Jaalouk, C.M. Shanahan, B. Burke, K.J. Roux, and J. Lammerding. 2011. The interaction between nesprins and sun proteins at the nuclear envelope is critical for force transmission between the nucleus and cytoskeleton. *J. Biol. Chem.* 286:26743–26753. https://doi.org/10.1074/jbc.M111.233700

Luxton, G.W., and G.G. Gundersen. 2011. Orientation and function of the nuclear-centrosomal axis during cell migration. *Curr. Opin. Cell Biol.* 23:579–588. https://doi.org/10.1016/j.ceb.2011.08.001

Luxton, G.W.G., E.R. Gomes, E.S. Folker, E. Vintinner, and G.G. Gundersen. 2010. Linear arrays of nuclear envelope proteins harness retrograde actin flow for nuclear movement. *Science.* 329:956–959.

Mandal, K., M. Balland, and L. Bureau. 2012. Thermoresponsive micropatterned substrates for single cell studies. *PLoS One.* 7:e37548. https://doi.org/10.1371/journal.pone.0037548

Mandal, K., I. Wang, E. Vitiello, L.A.C. Orellana, and M. Balland. 2014. Cell dipole behaviour revealed by ECM sub-cellular geometry. *Nat. Commun.* 5:5749. https://doi.org/10.1038/ncomms6749

Mason, B.N., A. Starchenko, R.M. Williams, L.J. Bonassar, and C.A. Reinhart-King. 2013. Tuning three-dimensional collagen matrix stiffness independently of collagen concentration modulates endothelial cell behavior. *Acta Biomater.* 9:4635–4644. https://doi.org/10.1016/j.actbio.2012.08.007

Meili, R., B. Alonso-Latorre, J.C. del Alamo, R.A. Firtel, and J.C. Lasheras. 2010. Myosin II is essential for the spatiotemporal organization of traction forces during cell motility. *Mol. Biol. Cell.* 21:405–417. https://doi.org/10.1091/mbc.E09-08-0703

Metzger, T., V. Gache, M. Xu, B. Cadot, E.S. Folker, B.E. Richardson, E.R. Gomes, and M.K. Baylies. 2012. MAP and kinesin-dependent nuclear positioning is required for skeletal muscle function. *Nature.* 484:120–124. https://doi.org/10.1038/nature10914

Nery, F.C., J. Zeng, B.P. Niland, J. Hewett, J. Farley, D. Irimia, Y. Li, G. Wiche, A. Sonnenberg, and X.O. Breakefield. 2008. TorsinA binds the KASH domain of nesprins and participates in linkage between nuclear envelope and cytoskeleton. *J. Cell Sci.* 121:3476–3486. https://doi.org/10.1242/jcs.029454

Padmakumar, V.C., T. Libotte, W. Lu, H. Zaim, S. Abraham, A.A. Noegel, J. Gotzmann, R. Foisner, and I. Karakesisoglou. 2005. The inner nuclear membrane protein Sun1 mediates the anchorage of Nesprin-2 to the nuclear envelope. *J. Cell Sci.* 118:3419–3430. https://doi.org/10.1242/jcs.02471

Pathak, A., and S. Kumar. 2012. Independent regulation of tumor cell migration by matrix stiffness and confinement. *Proc. Natl. Acad. Sci. USA.* 109:10334–10339. https://doi.org/10.1073/pnas.1118073109

Pelham, R.J. Jr., and Yl. Wang. 1997. Cell locomotion and focal adhesions are regulated by substrate flexibility. *Proc. Natl. Acad. Sci. USA.* 94:13661–13665. https://doi.org/10.1073/pnas.94.25.13661

Petrie, R.J., H. Koo, and K.M. Yamada. 2014. Generation of compartmentalized pressure by a nuclear piston governs cell motility in a 3D matrix. *Science.* 345:1062–1065.

Petrie, R.J., H.M. Harlin, L.I.T. Korsak, and K.M. Yamada. 2017. Activating the nuclear piston mechanism of 3D migration in tumor cells. *J. Cell Biol.* 216:93–100.

Peyton, S.R., and A.J. Putnam. 2005. Extracellular matrix rigidity governs smooth muscle cell motility in a biphasic fashion. *J. Cell. Physiol.* 204:198–209. https://doi.org/10.1002/jcp.20274

Piel, M., P. Meyer, A. Khodjakov, C.L. Rieder, and M. Bornens. 2000. The respective contributions of the mother and daughter centrioles to centrosome activity and behavior in vertebrate cells. *J. Cell Biol.* 149:317–330. https://doi.org/10.1083/jcb.149.2.317

Plotnikov, S.V., A.M. Pasapera, B. Sabass, and C.M. Waterman. 2012. Force fluctuations within focal adhesions mediate ECM-rigidity sensing to guide directed cell migration. *Cell.* 151:1513–1527. https://doi.org/10.1016/j.cell.2012.11.034

Raab, M., J. Swift, P.C.D.P. Dingal, P. Shah, J.-W. Shin, and D.E. Discher. 2012. Crawling from soft to stiff matrix polarizes the cytoskeleton and phosphoregulates myosin-II heavy chain. *J. Cell Biol.* 199:669–683. https://doi.org/10.1083/jcb.201205056

Raab, M., M. Gentili, H. de Belly, H.R. Thiam, P. Vargas, A.J. Jimenez, F. Lautenschlaeger, R. Voituriez, A.M. Lennon-Duménil, N. Manel, and M. Piel. 2016. ESCRT III repairs nuclear envelope ruptures during cell migration to limit DNA damage and cell death. *Science.* 352:359–362.

Ridley, A.J., M.A. Schwartz, K. Burridge, R.A. Firtel, M.H. Ginsberg, G. Borisy, J.T. Parsons, and A.R. Horwitz. 2003. Cell migration: integrating signals from front to back. *Science.* 302:1704–1709. https://doi.org/10.1126/science.1092053

Rommerswinkel, N., B. Niggemann, S. Keil, K.S. Zänker, and T. Dittmar. 2014. Analysis of cell migration within a three-dimensional collagen matrix. *J. Vis. Exp.* 92:e51963.

Roux, K.J., M.L. Crisp, Q. Liu, D. Kim, S. Kozlov, C.L. Stewart, and B. Burke. 2009. Nesprin 4 is an outer nuclear membrane protein that can induce kinesin-mediated cell polarization. *Proc. Natl. Acad. Sci. USA.* 106:2194–2199. https://doi.org/10.1073/pnas.0808602106

Shaw, G., and D. Bray. 1977. Movement and extension of isolated growth cones. *Exp. Cell Res.* 104:55–62. https://doi.org/10.1016/0014-4827(77)90068-4

Stewart, R.M., A.E. Zubek, K.A. Rosowski, S.M. Schreiner, V. Horsley, and M.C. King. 2015. Nuclear-cytoskeletal linkages facilitate cross talk between the nucleus and intercellular adhesions. *J. Cell Biol.* 209:403–418. https://doi.org/10.1083/jcb.201502024

Sunyer, R., V. Conte, J. Escribano, A. Elosegui-Artola, A. Labernadie, L. Valon, D. Navajas, J.M. García-Aznar, J.J. Muñoz, P. Roca-Cusachs, and X. Trepat. 2016. Collective cell durotaxis emerges from long-range inter-cellular force transmission. *Science.* 353:1157–1161.

Swift, J., I.L. Ivanovska, A. Buxboim, T. Harada, P.C.D.P. Dingal, J. Pinter, J.D. Pajerowski, K.R. Spinler, J.-W. Shin, M. Tewari, et al. 2013. Nuclear lamin-A scales with tissue stiffness and enhances matrix-directed differentiation. *Science.* 341:1240104.

Thakar, K., C.K. May, A. Rogers, and C.W. Carroll. 2017. Opposing roles for distinct LINC complexes in regulation of the small GTPase RhoA. *Mol. Biol. Cell.* 28:182–191.

Théry, M., V. Racine, M. Piel, A. Pépin, A. Dimitrov, Y. Chen, J.-B. Sibarita, and M. Bornens. 2006. Anisotropy of cell adhesive microenvironment governs cell internal organization and orientation of polarity. *Proc. Natl. Acad. Sci. USA.* 103:19771–19776. https://doi.org/10.1073/pnas.0609267103

Uetrecht, A.C., and J.E. Bear. 2009. Golgi polarity does not correlate with speed or persistence of freely migrating fibroblasts. *Eur. J. Cell Biol.* 88:711–717. https://doi.org/10.1016/j.ejcb.2009.08.001

Uzer, G., W.R. Thompson, B. Sen, Z. Xie, S.S. Yen, S. Miller, G. Bas, M. Styner, C.T. Rubin, S. Judex, et al. 2015. Cell mechanosensitivity to extremely low magnitude signals is enabled by a LINCed nucleus. *Stem Cells.* 33:2063–2076.

van Loosdregt, I.A.E.W., M.A.F. Kamps, C.W.J. Oomens, S. Loerakker, J.L.V. Broers, and C.V.C. Bouten. 2017. Lmna knockout mouse embryonic fibroblasts are less contractile than their wild-type counterparts. *Integr. Biol.* 9:709–721.

Verkhovsky, A.B., T.M. Svitkina, and G.G. Borisy. 1999. Self-polarization and directional motility of cytoplasm. *Curr. Biol.* 9:11–20.

Wang, N., J.D. Tytell, and D.E. Ingber. 2009. Mechanotransduction at a distance: mechanically coupling the extracellular matrix with the nucleus. *Nat. Rev. Mol. Cell Biol.* 10:75–82. https://doi.org/10.1038/nrm2594

Wigler, M.H., and I.B. Weinstein. 1975. A preparative method for obtaining enucleated mammalian cells. *Biochem. Biophys. Res. Commun.* 63:669–674. https://doi.org/10.1016/S0006-291X(75)80436-0

Wolf, K., M. Te Lindert, M. Krause, S. Alexander, J. Te Riet, A.L. Willis, R.M. Hoffman, C.G. Figdor, S.J. Weiss, and P. Friedl. 2013. Physical limits of cell migration: control by ECM space and nuclear deformation and tuning by proteolysis and traction force. *J. Cell Biol.* 201:1069–1084. https://doi.org/10.1083/jcb.201210152

Wu, C., S.B. Asokan, M.E. Berginski, E.M. Haynes, N.E. Sharpless, J.D. Griffith, S.M. Gomez, and J.E. Bear. 2012. Arp2/3 is critical for lamellipodia and response to extracellular matrix cues but is dispensable for chemotaxis. *Cell.* 148:973–987. https://doi.org/10.1016/j.cell.2011.12.034

Zhang, X., K. Lei, X. Yuan, X. Wu, Y. Zhuang, T. Xu, R. Xu, and M. Han. 2009. SUN1/2 and Syne/Nesprin-1/2 complexes connect centrosome to the nucleus during neurogenesis and neuronal migration in mice. *Neuron.* 64:173–187. https://doi.org/10.1016/j.neuron.2009.08.018